Micro-mechano-morphology-informed continuum damage modeling with intrinsic 2nd gradient (pantographic) grain–grain interactions

Luca Placidi, Dmitry Timofeev, Valerii Maksimov, Emilio Barchiesi, Alessandro Ciallella, Anil Misra, Francesco Dell'isola

Micro-mechano-morphology-informed continuum damage modeling with intrinsic 2nd gradient (pantographic) grain–grain interactions

Luca Placidi [a], Dmitry Timofeev [b], Valerii Maksimov [a], Emilio Barchiesi [c,d], Alessandro Ciallella [b], Anil Misra [e], Francesco dell'Isola [b]

[a] Faculty of Engineering, International Telematic University UNINETTUNO, Rome, Italy
[b] International Research Center on Mathematics and Mechanics of Complex Systems (M&MoCS), Università degli Studi dell'Aquila, L'Aquila, Italy
[c] École Nationale d'Ingénieurs de Brest, ENIB, UMR CNRS 6027, IRDL, F-29200 Brest, France
[d] Université de Bretagne Sud, IRDL-UBS - UMR CNRS 6027, Centre de Recherche, Rue de Saint Maudé - BP 92116 56321, Lorient, Cedex, France
[e] Civil, Environmental and Architectural Engineering Department, The University of Kansas, Kansas City, KS, USA

ABSTRACT

In a previous work, we have shown that a granular micromechanics approach can lead to load path dependent continuum models. In the present work, we generalize such a micromechanical approach introducing an intrinsic 2nd gradient energy storage mechanism (resembling pantographic micromechanism), in the grain–grain interaction. Such a mechanism, represents long-range effects but could also be thought as deriving from the utilization of an actual pantographic connection between two grains in a granular metamaterial. Taking advantage of the homogenization approach developed in previous works, we determine the mechanical behavior of the macro-scale continuum and carry out parametric analyses with respect to the averaged intergranular distance and with respect to the stiffness associated to the pantographic term. We show that with the inclusion of the pantographic term mentioned above, the desired thickness of the localization zone can be modeled and finely tuned successfully. We also show that the complex mechanics of load-path dependency can be predicated by the micromechanical effects and the introduced pantographic term.

1. Introduction

Damage and fracture can significantly impair the safety and operational capacity of many engineering devices and structures. Occurrence of damage often represents the extreme load scenario that drives the design. Therefore, resilience of modern engineering architectures with respect to damage, especially in critical applications like aeronautics, civil engineering and mechanical engineering, is often one of the main cost-driving factors.

Since it is often difficult and economically nonviable to validate (Oberkampf et al., 2004; Schwer, 2007; Babuska and Oden, 2004; TMS, 2019) by experimental means the real damage tolerance of a new architecture apart from scaled-down trials, with the design load cases often remaining untested, there is an increasing need for reliable modeling and related numerical protocols helping towards the objective above. One of the main challenges in damage mechanics is that loss of stiffness and failure of mechanical systems are often accompanied by localization of deformation (Placidi et al., 2018a,b). It is well known that numerical simulation of such problems utilizing methods such as classical fracture mechanics or classical damage mechanics presents serious shortcomings. For example, classical linear elastic fracture mechanics is unable to predict weakening or nucleation of defects at locations away from existing cracks, such as from boundaries that could appear, among others, due to material damage or weakness and related localization of deformation (Tokaji et al., 1987; Pook, 2000). Similarly, classical damage mechanics suffers from instabilities associated with loss of ellipticity, which typically requires certain regularization, particularly for simulating coalescence of microfractures into concentrated zones and for producing results that are independent of mesh size and shape used in numerical simulations (Kumar et al., 2020; Tanné et al., 2018; Fang et al., 2020; Carrara et al., 2020; Brach et al., 2019).

In recent years, phase-field models that include regularization have been proposed to address some of the above-mentioned shortcomings (Molnár et al., 2020; Miehe et al., 2016). However, further developments are needed, as many of these existing methods, including phase field methods, do not treat the effect of load paths and pre-loading upon the fracture paths and their evolution (Nguyen et al., 2020; Ouali et al., 2021). Moreover, localization zones (or shear bands) and boundary layers observed in many experiments are of finite spatial dimension and

they exist irrespective of the size of the domain (size of the structure). Regularization approaches proposed within the above mentioned classical and phase field approaches do not address the question of size of the localization zone, particularly from a micro-mechano-morphological viewpoint. In addition, in many past micro-macro identification, the 2nd gradient energy derived from lattice or discrete models depends upon the 1st gradient energy, and the 2nd gradient stiffnesses are proportional to 1st gradient ones and to the square of the RVE or to the lattice size (Askes and Metrikine, 2005; Askes and Aifantis, 2011; Chang and Gao, 1995; Maranganti and Sharma, 2007; Triantafyllidis and Bardenhagen, 1993). In these cases, and in the limit of such a size going to zero, the 2nd gradient constants vanish. Such schemes, therefore, cannot ex in that limit (i) a finite localization zone, that is in fact independent on grain sizes, and (ii) the fact that similar grain sizes lead to different shear band thickness (Jia et al., 2003; Polyzos and Fotiadis, 2012), an observation that can be attributed to correct micro-macro identification of kinematical features, including the effect of grain-rotation and other long-range effects. It is also noteworthy that strain localization could be accompanied by band broadening (Joshi and Ramesh, 2008) due to the evolution of micro-mechano-morphological effects an aspect that conventional fracture mechanics or shear band modeling largely overlooks (Placidi et al., 2019). To develop an approach in which we can incorporate the dependence upon the load-path and be able to regulate the localization zone thickness we utilize the micro-macro identification formalism based upon granular micromechanics (Misra et al., 2021; Placidi et al., 2021), in which it is considered that the elastic strain energy is stored and/or energy is dissipated in the deformation mechanisms representing interaction of grain-pairs. Such a deformation is modeled by relative motions of grain bary-centers, regardless of the location of the actual deformation within the grains.

It should be noted that, owing to recent advances in versatile manufacturing techniques as additive manufacturing allowing for their rapid production (Seppecher et al., 2019; Golaszewski et al., 2019; Spagnuolo et al., 2019; Trippel et al., 2020), architected materials, also known as metamaterials (Carcaterra et al., 2015; Del Vescovo and Giorgio, 2014; dell'Isola et al., 2016a), have become widespread in several fields of engineering. Indeed, properly designed architected materials can exhibit extremely favorable mechanical performances like low weight-to-stiffness ratios (Zheng et al., 2014; Giorgio et al., 2020a), high element-failure tolerance (Turco et al., 2016; Turco and Rizzi, 2016), and high energy-absorption capability (Mohsenizadeh et al., 2018). This has further urged theoretical mechanicians to take into account the significance of micro-scale mechanisms in influencing macro-scale material behaviors. Indeed, the main idea underlying the development of so-called metamaterials is the production of materials with artificially-controlled architecture conferring desired properties to the material (Yildizdag et al., 2019). Recently, the homogenization of different pantographic motifs (dell'Isola et al., 2016b; Rahali et al., 2015; Coutris et al., 2020; Boutin et al., 2017; dell'Isola et al., 2019), i.e. a mechanism which is well known from everyday life (pantographic mirrors, expanding fences, scissor lifts, etc.), which is characterized by a zero-energy accordion-like homogeneous extension/compression deformation mode, has been addressed for this reason. The studies on the homogenization of the above-mentioned pantographic motifs has concluded that, at macro-scale, they behave as second gradient continua. More particularly, the deformation energy of pantographic beams (Turco, 2019, 2021; Turco et al., 2021), i.e. slender pantographic structures, in contrast to the Elastica for which the deformation energy depends on the projection of the second gradient to the normal vector of the placement function, i.e. the material curvature, does also depend on the projection onto the tangent vector, introduced as the stretch gradient. Thus, the deformation energy takes into account the complete second gradient of the placement function. In such a model, non-standard boundary conditions and more generalized forces such as double forces do appear (Barchiesi et al., 2019, 2018). In other words, pantographic beams exhibit second gradient effects, i.e. non-locality or second-neighbor interactions, also in extension/compression and not only in bending, as standard beam models.

In previous works, we have proved that a granular micromechanics approach can lead to load path dependent outcomes (Placidi et al., 2021; Timofeev et al., 2020). Here, we generalize the grain-pair interaction by introducing an additional pantographic energy storage mechanism that depends upon strain gradient, and therefore, represents long-range (beyond nearest neighbor) effects that characterize all discrete systems and that need to be accounted for continuum models to be representative. More specifically, a spring is introduced at the micro-scale accumulating energy upon the gradient of its stretch, which can be regarded at a lower scale as a pantographic beam with fixed stretch at boundaries, deforming mainly along the axial direction, e.g. with low slenderness. Such a pantographic term generalizing the grain-pair interaction could be regarded not just as accounting generically for long-range interactions, but as a term deriving from the modeling of an actual pantographic sub-structure embedded within grain–grain interactions, that could be realized by 3D printing in the context of an actual granular metamaterial (Giorgio et al., 2020b; Misra et al., 2020; De Angelo et al., 2020; Nejadsadeghi et al., 2019).

In this paper, we show through numerical examples that with the inclusion of the pantographic term mentioned above, a micro-mechanical effects on the macro damage model is that the desired thickness of the localization zone can be modeled and finely tuned successfully. Moreover, the damaged state of the body subjected to complex loading paths can also described in a systematic way. In particular, the paper is organized as follows. In Section 2, the discrete micro-mechanical model for granular systems is introduced. The target continuum is introduced as well. Then, Piola's ansatz is employed to relate the discrete with the continuum and the objective relative grain–grain displacement is defined. Exploiting Piola's ansatz, continuum deformation measures are derived from the previously-introduced objective relative grain–grain displacement. Subsequently, stiffnesses and effective damaged stiffnesses are defined following the introduction of the kinematic damage descriptors for the state of degradation of each grain–grain interaction. In Section 3 the elastic strain energy associated to each grain–grain interaction is defined. Successively, in Section 4, the dissipation, external, and total energy functionals are introduced. After that, governing equations for the damage descriptors associated to each grain–grain interaction are derived from a variational deduction procedure based on a hemi-variational principle. Section 5 reports on the numerical results obtained by making use of the presented model. Particularly, parametric analyses are carried out with respect to the averaged intergranular distance and with respect to the stiffness associated to the pantographic term by re-scaling in micromechanical parameters with the averaged intergranular distance so to keep unchanged the continuum stiffness and damage characteristics.

2. Discrete and continuous descriptions of systems with grain–grain interactions

2.1. *Identification à la piola*

Within the discrete description, the reference configuration of the considered set of N grains is given by positions of their centroids

$$\boldsymbol{X}_i \in E^2, \text{ with } i = 1, \dots, N,$$

where E^2 is the Euclidean two-dimensional space. The position in the present (or current) configuration $\boldsymbol{x}_i \in E^2$, at time t, is obtained through the placement function $\chi_i(t)$ as follows

$$\boldsymbol{x}_i = \chi_i(t) = \boldsymbol{X}_i + \boldsymbol{u}_i(t), \qquad i = 1, \dots, N \tag{1}$$

where $\boldsymbol{u}_i(t)$ is the displacement function of the ith grain.

Within the continuum description, a continuous body $\mathcal{B} \subset E^2$, constituted by infinitely many particles, is considered in the reference

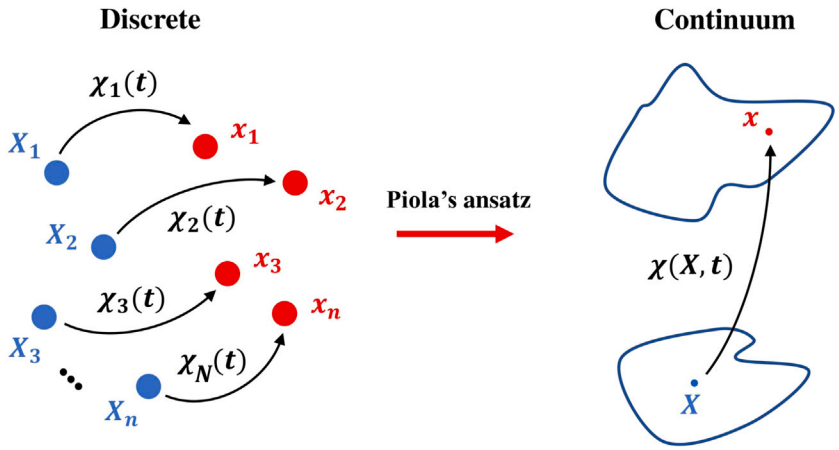

Fig. 1. Graphical representation of Piola's Ansatz in Eq. (3). Discrete kinematic descriptors introduced in Eq. (1), on the left, and continuous kinematic descriptor introduced in Eq. (2), on the right.

configuration. A generic particle occupies the position $\boldsymbol{X}$ in the reference configuration, i.e. $\boldsymbol{X} \in \mathcal{B}$. Such a particle is placed, in the present configuration at time t, into the position $\boldsymbol{x}$ through the placement function

$$\boldsymbol{x} = \boldsymbol{\chi}(\boldsymbol{X}, t) = \boldsymbol{X} + \boldsymbol{u}(\boldsymbol{X}, t), \tag{2}$$

where $\boldsymbol{u}(\boldsymbol{X}, t)$ is the displacement function of the continuous body $\mathcal{B}$.

In the continuum-discrete identification, the following relationship (Piola's Ansatz, see Fig. 1) will be assumed

$$\boldsymbol{\chi}(\boldsymbol{X}_i, t) = \boldsymbol{\chi}_i(t), \qquad i = 1, \dots, N, \tag{3}$$

which means that the placements $\boldsymbol{\chi}_i(t)$ of the N grains correspond to the placement $\boldsymbol{\chi}(\boldsymbol{X}, t)$ of the continuous body $\mathcal{B}$ evaluated at those positions $\boldsymbol{X} = \boldsymbol{X}_i$, with $i = 1, \dots, N$, where the grains are located in the reference configuration.

2.2. Objective relative grain–grain displacement and continuum deformation measures

Let us now consider just a pair of grains denoted as n and p with their centroids positioned at $\boldsymbol{X}_n$ and $\boldsymbol{X}_p$, respectively. Let us also assume that the distance between them is equal to L, that is assumed to be the averaged intergranular distance. Furthermore, the unit vector $\hat{\boldsymbol{c}}$ can be defined as follows

$$\boldsymbol{X}_n - \boldsymbol{X}_p = \hat{\boldsymbol{c}} L. \tag{4}$$

Therefore, the vector quantity $\hat{\boldsymbol{c}} L$ in Eq. (4) is nothing but the arrow in the reference configuration that, once applied to the position $\boldsymbol{X}_n$, touches and points towards the position $\boldsymbol{X}_p$. In the current configuration, at time t, the positions occupied by the two grain centroids at positions $\boldsymbol{X}_n$ and $\boldsymbol{X}_p$ in the reference configuration are, respectively, $\boldsymbol{x}_n = \boldsymbol{\chi}(\boldsymbol{X}_n, t)$ and $\boldsymbol{x}_p = \boldsymbol{\chi}(\boldsymbol{X}_p, t)$. Analogously, the vector in Eq. (4) is transformed in the present configuration, at time t, into

$$\boldsymbol{x}_n - \boldsymbol{x}_p = \boldsymbol{\chi}(\boldsymbol{X}_n, t) - \boldsymbol{\chi}(\boldsymbol{X}_p, t). \tag{5}$$

Following (Timofeev et al., 2020), an objective relative displacement is defined as

$$\boldsymbol{u}^{np} = \boldsymbol{F}^T (\boldsymbol{x}_n - \boldsymbol{x}_p) - (\boldsymbol{X}_n - \boldsymbol{X}_p), \tag{6}$$

where $\boldsymbol{F} = \nabla \boldsymbol{\chi}$ is the deformation gradient. Here and after ∇ means the gradient operator with respect to the position X in the reference configuration.

Let us now assume that the two grains n and p are neighboring ones. Thus, the Taylor's series expansion of the function $\boldsymbol{\chi}(\boldsymbol{X}_n, t)$ centered at $\boldsymbol{X} = \boldsymbol{X}_p$ yields

$$\boldsymbol{x}_n = \boldsymbol{\chi}(\boldsymbol{X}_n, t) \cong \boldsymbol{x}_p + L \boldsymbol{F}_p \hat{\boldsymbol{c}} + \frac{L^2}{2} \left[\nabla_p \boldsymbol{F} \hat{\boldsymbol{c}}\right] \cdot \hat{\boldsymbol{c}}, \tag{7}$$

where the following second and third order tensors evaluated at $\boldsymbol{X} = \boldsymbol{X}_p$ have been defined

$$\boldsymbol{F}_p = (\nabla \boldsymbol{\chi})_{\boldsymbol{X}=\boldsymbol{X}_p}, \qquad \nabla_p \boldsymbol{F} = [\nabla (\nabla \boldsymbol{\chi})]_{\boldsymbol{X}=\boldsymbol{X}_p}.$$

Let us also introduce the Green-Saint-Venant tensor $\boldsymbol{G}$ and its gradient, which are, respectively, a second and third order tensor

$$\boldsymbol{G} = \frac{1}{2}\left(\boldsymbol{F}^T \boldsymbol{F} - \boldsymbol{I}\right), \quad \nabla \boldsymbol{G} = \boldsymbol{F}^T \nabla \boldsymbol{F}. \tag{8}$$

Eqs. (7) and (8), in index notation, where superscripts denote the position at which the corresponding quantity is evaluated, read as

$$\begin{aligned} &x_i^n = x_i^p + F_{ij}^p \hat{c}_j L + \frac{L^2}{2} F_{ij,h}^p \hat{c}_j \hat{c}_h, \quad G_{ij}^p = \frac{1}{2}\left(F_{ai}^p F_{aj}^p - \delta_{ij}\right), \\ &G_{ij,h}^p = F_{ai}^p F_{aj,h}^p. \end{aligned} \tag{9}$$

Thus, making use of the index notation and taking into account Eqs. (4) and (9), the objective relative displacement in Eq. (6) can be re-written as

$$u_i^{np} = 2 G_{ij}^p \hat{c}_j L + \frac{L^2}{2} G_{ij,h}^p \hat{c}_j \hat{c}_h. \tag{10}$$

We remark that, owing to Eq. (10), the objective relative displacement $\boldsymbol{u}^{np}$ for a given grain–grain orientation $\hat{\boldsymbol{c}}$ is not additive inverse of that computed for the opposite grain–grain orientation, i.e. $-\hat{\boldsymbol{c}}$, when the strain gradient is non-vanishing, i.e. $\nabla \boldsymbol{G} \neq 0$, because it is not an odd function of $\hat{\boldsymbol{c}}$. This means that the strain gradient breaks the symmetry with respect to the inversion of the grain–grain orientation. Such a feature enables strain-gradient-triggered chiral effects.

The half-projection of the objective relative displacement on the unit vector $\hat{\boldsymbol{c}}$ is the so-called normal displacement u_η (a scalar quantity), while its projection on the unit vector orthogonal to $\hat{\boldsymbol{c}}$ is the so-called tangent displacement vector

$$u_\eta = \frac{1}{2} \boldsymbol{u}^{np} \cdot \hat{\boldsymbol{c}}, \quad \boldsymbol{u}_\tau = \boldsymbol{u}^{np} - (\boldsymbol{u}^{np} \cdot \hat{\boldsymbol{c}})\, \hat{\boldsymbol{c}}. \tag{11}$$

Such a definition for u_η have been chosen in order to have non-confusing interpretation of stiffness parameters defined in the next subsection. For the detailed justification one can see Placidi et al. (2021). Insertion of (10) into (11) yields the normal displacement, its square and the squared tangent displacements, in terms of the strain $\boldsymbol{G}$, the strain gradient $\nabla \boldsymbol{G}$, the grain–grain distance L and its orientation $\hat{\boldsymbol{c}}$

$$u_\eta = L G_{ij} \hat{c}_i \hat{c}_j + \frac{L^2}{4} G_{ij,h} \hat{c}_i \hat{c}_j \hat{c}_h, \tag{12}$$

$$\begin{aligned} u_\eta^2 &= L^2 \hat{c}_i \hat{c}_j \hat{c}_a \hat{c}_b G_{ij} G_{ab} + \frac{1}{2} L^3 \hat{c}_i \hat{c}_j \hat{c}_a \hat{c}_b \hat{c}_c G_{ij} G_{ab,c} \\ &+ \frac{1}{16} L^4 \hat{c}_i \hat{c}_j \hat{c}_h \hat{c}_a \hat{c}_b \hat{c}_c G_{ij,h} G_{ab,c}, \end{aligned} \tag{13}$$

$$u_\tau^2 = 4L^2 G_{ij} G_{ab} \left(\delta_{ia}\hat{c}_j\hat{c}_b - \hat{c}_i\hat{c}_j\hat{c}_a\hat{c}_b\right) + 2L^3 G_{ij} G_{ab,c} \left(\delta_{ia}\hat{c}_j\hat{c}_b\hat{c}_c - \hat{c}_i\hat{c}_j\hat{c}_a\hat{c}_b\hat{c}_c\right) + \frac{L^4}{4} G_{ij,h} G_{am,n} \left(\delta_{ia}\hat{c}_j\hat{c}_h\hat{c}_m\hat{c}_n - \hat{c}_i\hat{c}_j\hat{c}_h\hat{c}_a\hat{c}_b\hat{c}_c\right), \tag{14}$$

where the superscript p has been omitted to simplify the notation.

2.3. Damage descriptors and effective stiffnesses

Following the same notation employed in Timofeev et al. (2020), the damaged tangent stiffness is denoted with $k_{\tau,D}$ and the damaged normal stiffness is denoted with $k_{\eta,D}$

$$k_{\eta,D} = k_{\eta,D}^t \Theta\left(u_\eta\right) + k_{\eta,D}^c \Theta\left(-u_\eta\right), \tag{15}$$

where $k_{\eta,D}^t$ is the stiffness in tension and $k_{\eta,D}^c \gg k_{\eta,D}^t$ is the stiffness in compression. Remark that, usually, for cementitious granular materials the stiffness in compression is much higher than the stiffness in tension. Here, tension and compression are discriminated through the sign of the objective normal displacement u_η and, for this reason, we make use of the Heaviside function Θ. Damage is modeled with two variables, i.e. the normal damage D_η, and the tangent damage D_τ. The damage variables D_η and D_τ reduce linearly, respectively, the tension and compression normal damaged stiffness $k_{\eta,D}$(15) and the tangent damaged stiffness $k_{\tau,D}$. In formulas, we have

$$k_{\eta,D}^t = k_\eta^t\left(1 - D_\eta\right), \qquad k_{\eta,D}^c = k_\eta^c\left(1 - D_\eta\right), \qquad k_{\tau,D} = k_\tau\left(1 - D_\tau\right), \tag{16}$$

which means that the tangent damaged stiffness $k_{\tau,D}$ and the normal damaged stiffness $k_{\eta,D}$ are defined, respectively, through the non-damaged tangent stiffness k_τ and the non-damaged normal stiffness k_η. For the latter case, in formulas, we have $k_{\eta,D} = k_\eta\left(1 - D_\eta\right)$, where the non-damaged normal stiffness k_η has been defined in terms of the non-damaged tension normal stiffness k_η^t and the non-damaged compression normal stiffness k_η^c as

$$k_\eta = k_\eta^t \Theta\left(u_\eta\right) + k_\eta^c \Theta\left(-u_\eta\right). \tag{17}$$

We hence obtain the following synthetic expression for the damaged normal stiffness

$$k_{\eta,D} = k_\eta\left(1 - D_\eta\right) = k_\eta^t\left(1 - D_\eta\right)\Theta\left(u_\eta\right) + k_\eta^c\left(1 - D_\eta\right)\Theta\left(-u_\eta\right). \tag{18}$$

In order to smooth the constitutive assumption in Eq. (17), the Heaviside function $\Theta(x)$ is replaced in the numerical scheme by the following smooth function (see Fig. 2) (Wang and Qian, 2018)

$$\frac{1}{2} + \frac{1}{\pi}\arctan\left(\frac{x}{\alpha}\right) \tag{19}$$

so that the non-damaged normal stiffness is defined as a smooth function of the normal relative displacement

$$k_\eta = \frac{1}{2}\left(k_\eta^t + k_\eta^c\right) + \frac{1}{\pi}\left(k_\eta^t - k_\eta^c\right)\arctan\left(\frac{u_\eta}{\alpha}\right), \tag{20}$$

that in turns gives the damaged normal stiffness as a smooth function of the normal relative displacement

$$k_{\eta,D} = \frac{1}{2}\left(k_\eta^t + k_\eta^c\right)\left(1 - D_\eta\right) + \frac{1}{\pi}\left(k_\eta^t - k_\eta^c\right)\arctan\left(\frac{u_\eta}{\alpha}\right)\left(1 - D_\eta\right). \tag{21}$$

The quantity α can be tuned to modulate the regularization. Large values of α enhance the convergence of the algorithm. A value for α is considered, see Table 1, as to give a sufficiently smooth and non-stiff problem while not being detrimental to the congruence of Eqs. (17), (20) and (18), (21), so that the physical meaning of α can be overlooked.

3. Elastic strain energy

The elastic energy density per unit area is derived starting from the elastic energy associated to a single grain–grain interaction, say the couple $n - p$ considered in Section 2.2, within the discrete description. It is chosen to be additively decomposed in two parts

$$U^{tot} = U_u + U_P,$$

where the first contribution U_u follows the modeling assumption of Timofeev et al. (2020)

$$U_u = \frac{1}{2}k_{\eta,D}u_\eta^2 + \frac{1}{2}k_{\tau,D}u_\tau^2, \tag{22}$$

having intergranular interaction described by means of normal and tangential springs. It is worth to be noted that the damaged elastic stiffnesses in Eqs. $(16)_3$ and (18), which are related to those springs, can be defined as the coefficients of a quadratic form of the objective normal and tangential displacements in Eq. (22).

The second term U_P reads as

$$U_P = \frac{1}{2}K_P\left[\left(\nabla u_\eta\right)\cdot\hat{c}\right]^2 \tag{23}$$

and it is introduced as an additional energy storage mechanism that represents long-range (beyond nearest neighbor) effects, and therefore, upon gradients of relative displacement. The normal gradient of the objective normal displacement is, neglecting second gradient of strain terms,

$$\left(\nabla u_\eta\right)\cdot\hat{c} = LG_{ij,h}^p\hat{c}_i\hat{c}_j\hat{c}_h$$

and it leads us to the U_P formulation in terms of strain gradient components

$$U_P = \frac{1}{2}K_P\left[\left(\nabla u_\eta\right)\cdot\hat{c}\right]^2 = \frac{1}{2}K_P L^2 G_{ij,h}^p G_{ab,c}^p \hat{c}_i\hat{c}_j\hat{c}_h\hat{c}_a\hat{c}_b\hat{c}_c. \tag{24}$$

The grain–grain interaction is, therefore, no longer represented by two (normal and tangential) springs. The introduction of the term U_P allows us to account, for instance, for a non-null strain energy when the objective relative displacement $\boldsymbol{u}^{np}$ is zero for both normal u_η and tangential u_τ components. It can be seen from Fig. 3 that such a behavior resembles that of a pantograph. Thus, the introduction of U_P implies a kind of pantographic interaction mechanism and the coefficient K_P will be further referred to as the coefficient of pantographic interaction (or the pantographic coefficient).

In the discrete description, the total energy U^{tot} associated to the interaction of a given grain, whose centroid occupies the position $\boldsymbol{X}_p$ in the reference configuration, with neighboring grains is given by the summation of the energy in Eq. (22) for all the $N - 1$ possible interactions

$$U^{tot} = \sum_{i=1}^{N-1} U_i = \sum_{i=1}^{N-1}\left(U_{u,i} + U_{P,i}\right) = \sum_{i=1}^{N-1}\left(\frac{1}{2}k_{\eta,D,i}u_{\eta,i}^2 + \frac{1}{2}k_{\tau,D,i}u_{\tau,i}^2 + \frac{1}{2}K_{P,i}\left[\left(\nabla u_{\eta,i}\right)\cdot\hat{c}_i\right]^2\right), \tag{25}$$

where the subscript i refers to a generic couple n–p of grains. In Eq. (25) it is therefore intended that $k_{\eta,D,i}$ and $k_{\tau,D,i}$ are the damaged stiffnesses, respectively normal and tangent, associated to the interaction of the ith couple of grains, while $u_{\eta,i}^2$ and $u_{\tau,i}^2$ are the squared elastic relative displacements, respectively normal and tangent, of the ith couple of grains. By $\left[\left(\nabla u_{\eta,i}\right)\cdot\hat{c}_i\right]^2$ we denoted the squared normal gradient of objective normal displacement of the ith couple of grains.

It is worth to mention here that the pantographic coefficients $K_{P,i}$ are not affected by damage growth, in contrast to other stiffnesses in Eq. (25), so the term U_P remains finite during the evolution of the system.

Continualization of Eq. (25) is performed by using the following homogenization rule (see Fig. 4). Let a be a generic quantity defined within the discrete description, such that a_i refers to the grain–grain

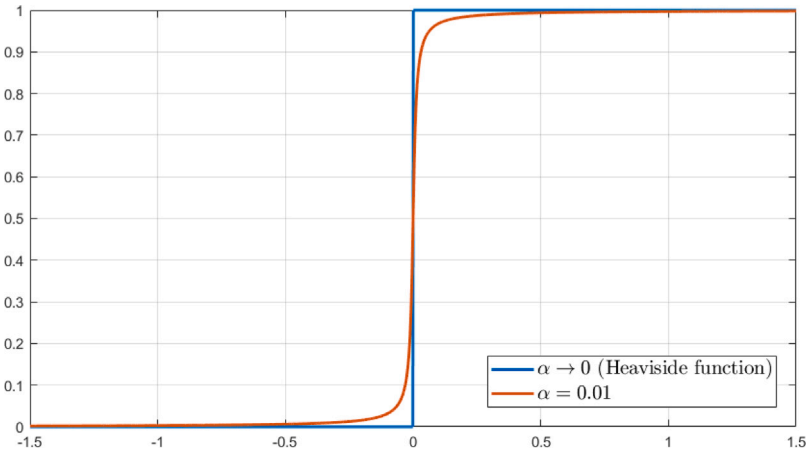

Fig. 2. Plot for Eq. (19). In the limit of α going to zero the smooth function in (19) goes to the Heaviside function.

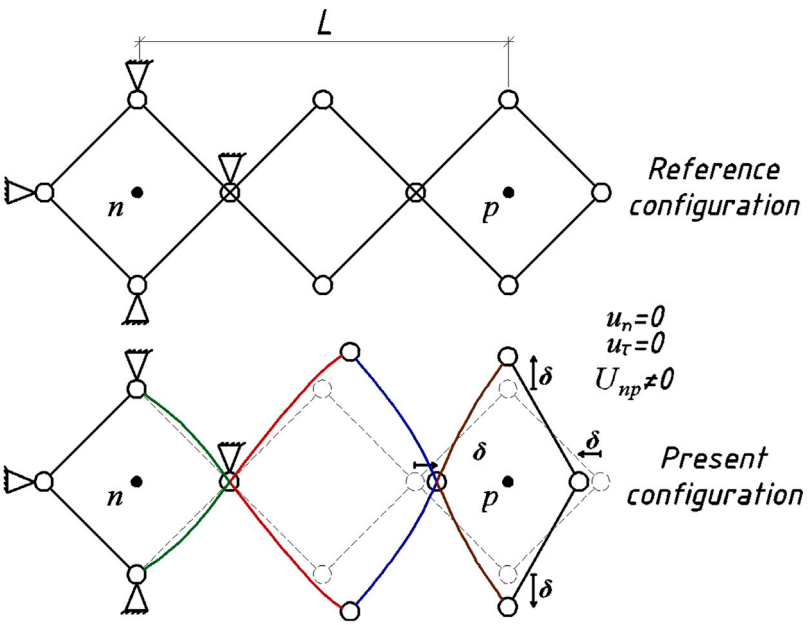

Fig. 3. Representation of the pantographic mechanism.

interaction, identified with the index i, between a generic grain n and a generic grain p. Let $a(\theta)$ be the continuous distribution of the quantity a over the orientation θ of the grain-pair formed by grain n and its neighboring grains. We have that, when the number N of grains within the discrete system tends to infinite, the following limit holds

$$\sum_{i=1}^{N} [a_i] \quad \longrightarrow \quad \int_{S^1} a(\theta)\,, \tag{26}$$

where $S^1 = [0, 2\pi]$ is the unit circle, namely the domain of the function $a(\theta)$, i.e. the set of all orientations. Remark that $a_i = a(\theta_i)$, where θ_i is the orientation of the grain-pair formed by grain n and grain p, namely the orientation of the unit vector $\hat{c}$. The application of the homogenization rule in Eq. (26) to the total energy U^{tot} in Eq. (25) gives

$$U^{tot} \quad \longrightarrow \quad U = \int_{S^1} \frac{1}{2} k_\eta \left(1 - D_\eta\right) u_\eta^2 + \frac{1}{2} k_\tau \left(1 - D_\tau\right) u_\tau^2, \\ + \frac{1}{2} K_P \left[\left(\nabla u_\eta\right) \cdot \hat{c}\right]^2, \tag{27}$$

where $k_\eta = \widetilde{k}_\eta(\theta)$, $k_\tau = \widetilde{k}_\tau(\theta)$, $K_P = \widetilde{K}_P(\theta)$, $D_\eta = \widetilde{D}_\eta(\theta)$, and $D_\tau = \widetilde{D}_\tau(\theta)$ replace, respectively, $k_{\eta,i}$, $k_{\tau,i}$, $K_{P,i}$, $D_{\eta,i}$, and $D_{\tau,i}$. Remark that these quantities are all functions of the orientation $\theta \in [0, 2\pi]$ of the generic grain-pair formed by grain n and its neighboring grains, namely

$$k_{\eta,i} \to \widetilde{k}_\eta(\theta)\,, \quad k_{\tau,i} \to \widetilde{k}_\tau(\theta)\,, \quad K_{p,i} \to \widetilde{K}_p(\theta) \quad D_{\eta,i} \to \widetilde{D}_\eta(\theta)\,, \\ D_{\tau,i} \to \widetilde{D}_\tau(\theta)\,.$$

From Eqs. (13) and (14) the continuum elastic strain energy density per unit area in Eq. (27) reads as

$$\begin{aligned} U = & \int_{S^1} \frac{1}{2} k_\eta \left(1 - D_\eta\right) \left(L^2 \hat{c}_i \hat{c}_j \hat{c}_a \hat{c}_b G_{ij} G_{ab} + \frac{1}{2} L^3 \hat{c}_i \hat{c}_j \hat{c}_a \hat{c}_b \hat{c}_c G_{ij} G_{ab,c}\right) \\ & + \int_{S^1} \frac{1}{2} k_\eta \left(1 - D_\eta\right) \left(\frac{1}{16} L^4 \hat{c}_i \hat{c}_j \hat{c}_h \hat{c}_a \hat{c}_b \hat{c}_c G_{ij,h} G_{ab,c}\right) \\ & + \int_{S^1} \frac{1}{2} k_\tau \left(1 - D_\tau\right) \left(4 L^2 G_{ij} G_{ab} \left(\delta_{ia} \hat{c}_j \hat{c}_b - \hat{c}_i \hat{c}_j \hat{c}_a \hat{c}_b\right)\right. \\ & \left. + 2 L^3 G_{ij} G_{ab,c} \left(\delta_{ia} \hat{c}_j \hat{c}_b \hat{c}_c - \hat{c}_i \hat{c}_j \hat{c}_a \hat{c}_b \hat{c}_c\right)\right) \\ & + \int_{S^1} \frac{1}{2} k_\tau \left(1 - D_\tau\right) \left(\frac{1}{4} L^4 G_{ij,h} G_{am,n} \left(\delta_{ia} \hat{c}_j \hat{c}_h \hat{c}_m \hat{c}_n - \hat{c}_i \hat{c}_j \hat{c}_h \hat{c}_a \hat{c}_b \hat{c}_c\right)\right) \\ & + \int_{S^1} \frac{1}{2} K_P L^2 G_{ij,h} G_{ab,c} \hat{c}_i \hat{c}_j \hat{c}_h \hat{c}_a \hat{c}_b \hat{c}_c. \end{aligned} \tag{28}$$

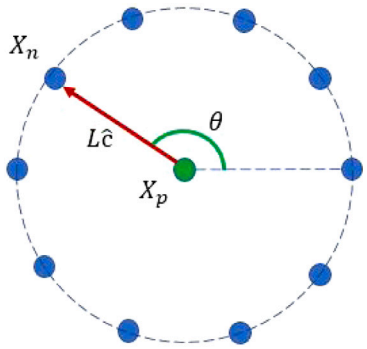

Fig. 4. Graphic representation of the homogenization rule.

The previous expression can be re-written in a more compact form as

$$U = \frac{1}{2}\mathbb{C}_{ijab}G_{ij}G_{ab} + \mathbb{M}_{ijabc}G_{ij}G_{ab,c} + \frac{1}{2}\mathbb{D}_{ijhabc}G_{ij,h}G_{ab,c}, \tag{29}$$

where, accounting for the symmetrization induced by the symmetry of the strain tensor $\boldsymbol{G}$, the elastic stiffnesses $\mathbb{C}$, $\mathbb{M}$, $\mathbb{D}$ are identified as follows

$$\mathbb{C}_{ijab} = L^2 \int_{S^1} k_\eta \left(1 - D_\eta\right) \hat{c}_i\hat{c}_j\hat{c}_a\hat{c}_b \tag{30}$$
$$+L^2 \int_{S^1} k_\tau \left(1 - D_\tau\right) \left(\left(\delta_{ia}\hat{c}_j\hat{c}_b + \delta_{ib}\hat{c}_j\hat{c}_a + \delta_{ja}\hat{c}_i\hat{c}_b + \delta_{jb}\hat{c}_i\hat{c}_a\right) - 4\hat{c}_i\hat{c}_j\hat{c}_a\hat{c}_b\right)$$

$$\mathbb{M}_{ijabc} = \frac{1}{4}L^3 \int_{S^1} k_\eta \left(1 - D_\eta\right) \hat{c}_i\hat{c}_j\hat{c}_a\hat{c}_b\hat{c}_c \tag{31}$$
$$\frac{1}{4}L^3 \int_{S^1} k_\tau \left(1 - D_\tau\right) \left(\left(\delta_{ia}\hat{c}_j\hat{c}_b + \delta_{ib}\hat{c}_j\hat{c}_a + \delta_{ja}\hat{c}_i\hat{c}_b + \delta_{jb}\hat{c}_i\hat{c}_a\right)\hat{c}_c$$
$$- 4\hat{c}_i\hat{c}_j\hat{c}_a\hat{c}_b\hat{c}_c\right)$$

$$\mathbb{D}_{ijhabc} = \frac{1}{16}L^4 \int_{S^1} k_\eta \left(1 - D_\eta\right) \hat{c}_i\hat{c}_j\hat{c}_h\hat{c}_a\hat{c}_b\hat{c}_c \tag{32}$$
$$+\frac{1}{16}L^4 \int_{S^1} k_\tau \left(1 - D_\tau\right) \left(\left(\delta_{ia}\hat{c}_j\hat{c}_b + \delta_{ib}\hat{c}_j\hat{c}_a + \delta_{ja}\hat{c}_i\hat{c}_b + \delta_{jb}\hat{c}_i\hat{c}_a\right)\hat{c}_h\hat{c}_c$$
$$- 4\hat{c}_i\hat{c}_j\hat{c}_h\hat{c}_a\hat{c}_b\hat{c}_c\right)$$
$$+ L^2K_P \int_{S^1} \hat{c}_i\hat{c}_j\hat{c}_h\hat{c}_a\hat{c}_b\hat{c}_c$$

From Eqs. (30)–(32) one can see the presence of the pantographic coefficient K_P only in the expression for the six-rank elastic stiffness tensor $\mathbb{D}$. Therefore, since neither D_η nor D_τ affects K_P, we can notice that all of the components of the elastic tensors $\mathbb{C}$ and $\mathbb{M}$ tend to zero because of damage growth, but for the elastic tensor $\mathbb{D}$ it is not true. Hence, there is always some portion of elastic energy stored at every material point of the continuum even if we assume the damage variables reaching their maximum values.

Let us finally remark that, from the nontrivial expression in Eq. (31) for the stiffness $\mathbb{M}$, it is not odd with respect to grain-pair's orientation. Thus, it is deduced that the occurrence of damage, induce the emergence of chiral effects. Note that, indeed, in the integral (31), the unit vector $\hat{c}$ appears an odd number of times, while the domain is symmetric with respect to zero. Thus, while initially we have $\mathbb{M} = \mathbf{0}$ the evolution of damage variables D_η and D_τ, induces the emergence of chiral effects characterized by the conditions $\mathbb{M} \neq \mathbf{0}$.

4. Evolution of damage descriptors

4.1. Definition of the fundamental kinematical quantities

We evaluate the evolution of damage variables via an hemi-variational derivation of the grain interaction, that is considered for a given orientation. To do this, we start by the definition of the following 4 (3 scalar and one vector) fundamental kinematical quantities

$$u_\eta, \boldsymbol{u}_\tau, D_\eta, D_\tau, \tag{33}$$

where u_η, $\boldsymbol{u}_\tau$, D_η and D_τ have been already defined in Eqs. (11) and (16).

4.2. Definition of the dissipation, external and total energy functionals

The dissipation energy W_D is the energy dissipated because of irreversible phenomena, which is damage in our case. It can be additively decomposed into normal, i.e. W_D^η, and tangent, i.e. W_D^τ, parts

$$W_D = W_D^\eta + W_D^\tau. \tag{34}$$

The normal contribution W_D^η to the damage dissipation energy is defined as follows

$$W_D^\eta = \frac{1}{2}k_\eta^c \left(B_\eta^c\right)^2 \Theta\left(-u_\eta\right)\left[-D_\eta + \frac{2}{\pi}\tan\left(\frac{\pi}{2}D_\eta\right)\right] + \tag{35}$$
$$\frac{1}{2}k_\eta^t \left(B_\eta^t\right)^2 \Theta\left(u_\eta\right)\left[2 + \left(D_\eta - 1\right)\left(2 - 2\log\left(1 - D_\eta\right) + \left(\log\left(1 - D_\eta\right)\right)^2\right)\right],$$

where B_η^c and B_η^t are two characteristic lengths associated to normal damage dissipation in compression and in tension, respectively. We observe that usually, for cementitious materials, we have $B_\eta^t \ll B_\eta^c$. Indeed, a much smaller amount of elastic relative displacement is needed in tension to activate damage mechanisms. The tangent contribution W_D^τ to the damage dissipation energy is defined as follows

$$W_D^\tau = \frac{1}{2}k_\tau \left[\widetilde{B}_\tau\left(u_\eta\right)\right]^2 \left[2 + \left(D_\tau - 1\right)\left(2 - 2\log\left(1 - D_\tau\right)\right.\right.$$
$$\left.\left. + \left(\log\left(1 - D_\tau\right)\right)^2\right)\right], \tag{36}$$

where $B_\tau = \widetilde{B}_\tau\left(u_\eta\right)$ is the characteristic length associated to tangent damage dissipation. Such a characteristic length is assumed to depend the normal relative grain–grain displacement, as in Misra and Poorsolhjouy (2015) and Misra and Singh (2015). Additionally, differently from Misra and Poorsolhjouy (2015) and Misra and Singh (2015) and for the sake of simplicity, the effect of the mean stress has been neglected. Following said references, the functional dependence $\widetilde{B}_\tau\left(u_\eta\right)$ has been chosen as follows

$$B_\tau = \widetilde{B}_\tau\left(u_\eta\right) = \begin{cases} B_{\tau 0} & \text{if } u_\eta \geq 0 \\ B_{\tau 0} - \alpha_2 u_\eta & \text{if } \frac{1-\alpha_1}{\alpha_2}B_{\tau 0} \leq u_\eta < 0 \\ \alpha_1 B_{\tau 0} & \text{if } u_\eta < B_{\tau 0}\frac{1-\alpha_1}{\alpha_2}, \end{cases} \tag{37}$$

where $B_{\tau 0}$ ($B_{\omega 0}$ in Misra and Poorsolhjouy (2015) and Misra and Singh (2015)), α_1 and α_2 are further constitutive parameters needed to express the functional dependence $\widetilde{B}_\tau\left(u_\eta^{el}\right)$. Such a functional dependence couples the two addends W_D^η and W_D^τ of the decomposition (34).

In conclusion, because of Eqs. (34), (35), (36), the dissipation energy functional (34) reads as

$$W = W_D^\eta + W_D^\tau \tag{38}$$
$$= \frac{1}{2}k_\eta^c\Theta\left(-u_\eta^{el}\right)B_c^2\left[-D_\eta + \tan\left(D_\eta\right)\right]$$
$$+ \frac{1}{2}k_\eta^t\Theta\left(u_\eta^{el}\right)B_t^2\left[2 + \left(D_\eta - 1\right)\left(2 - 2\log\left(1 - D_\eta\right) + \left(\log\left(1 - D_\eta\right)\right)^2\right)\right]$$
$$+ \frac{1}{2}k_\tau B_\tau^2\left[2 + \left(D_\tau - 1\right)\left(2 - 2\log\left(1 - D_\tau\right) + \left(\log\left(1 - D_\tau\right)\right)^2\right)\right]$$

Within the considered approach, the external world can exert forces expending power both on the scalar normal objective relative displacement u_η and on the vector tangent objective relative displacement $\boldsymbol{u}_\tau$, so that the external energy functional is

$$U^{ext} = F_\eta^{ext}u_\eta + F_\tau^{ext}\cdot\boldsymbol{u}_\tau, \tag{39}$$

where F_η^{ext} and F_τ^{ext} are, respectively, the external normal and tangent forces. Since we are neglecting kinetic energy and considering quasi-static evolution, the energy functional $\mathcal{E}$ reads as

$$\mathcal{E} = U + W - U^{ext}. \tag{40}$$

Remark that it is a functional of the fundamental kinematical quantities (33), namely

$$\mathcal{E} = \mathcal{E}\left(u_\eta, \boldsymbol{u}_\tau, D_\eta, D_\tau\right). \tag{41}$$

4.3. Formulation of the hemi-variational principle

The variational inequality principle can be here applied similarly to what has been done in Timofeev et al. (2020). We introduce a monotonously increasing time sequence $T_i \in \{T_i\}_{i=0,\dots,M}$ with $T_i \in \mathbb{R}$ and $M \in \mathbb{N}$. An initial datum on each of the fundamental kinematic quantities must be given for $i = 0$, i.e. for time T_0. A motion is defined as a family of displacements $\zeta = (u_\eta, \boldsymbol{u}_\tau)$ defined for each time $t = T_0, T_1, \dots, T_M$. The set AM_t is defined as the set of kinematically admissible displacements for a given time t — we require $(u_\eta, \boldsymbol{u}_\tau) \in AM_t$ — and the set AV_t is defined as the corresponding space of kinematically admissible variations — i.e. $\upsilon = (\delta u_\eta, \delta \boldsymbol{u}_\tau) \in AV_t$. Admissible variations β of the irreversible kinematic quantities (D_η, D_τ) must be positive, namely

$$\beta = \delta D_\eta, \delta D_\tau \in \mathbb{R}^+ \times \mathbb{R}^+. \tag{42}$$

The first variation $\delta\mathcal{E}$ of the energy functional (41) is defined as

$$\delta\mathcal{E} = \mathcal{E}\left(u_\eta + \delta u_\eta, \boldsymbol{u}_\tau + \delta \boldsymbol{u}_\tau, D_\eta + \delta D_\eta, D_\tau + \delta D_\tau\right) - \mathcal{E}\left(u_\eta, \boldsymbol{u}_\tau, D_\eta, D_\tau\right). \tag{43}$$

The increment of the fundamental kinematic quantities (33) at $t = T_i$ is given by the difference between these quantities as evaluated at times $t = T_i$ and $t = T_{i-1}$, namely

$$\left(\Delta u_\eta, \Delta \boldsymbol{u}_\tau, \Delta D_\eta, \Delta D_\tau\right)_{T_i} = \left(u_\eta, \boldsymbol{u}_\tau, D_\eta, D_\tau\right)_{T_i} - \left(u_\eta, \boldsymbol{u}_\tau, D_\eta, D_\tau\right)_{T_{i-1}}.$$

The same definition is utilized for the increment $\Delta\mathcal{E}$ of the energy functional

$$\Delta\mathcal{E} = \mathcal{E}\left(u_\eta + \Delta u_\eta, \boldsymbol{u}_\tau + \Delta \boldsymbol{u}_\tau, D_\eta + \Delta D_\eta, D_\tau + \Delta D_\tau\right) - \mathcal{E}\left(u_\eta, \boldsymbol{u}_\tau, D_\eta, D_\tau\right). \tag{44}$$

Finally, the hemi-variational principle is formulated as follows

$$\Delta\mathcal{E} \le \delta\mathcal{E} \quad \forall \upsilon = \left(\delta u_\eta, \delta \boldsymbol{u}_\tau\right) \in AV_t, \qquad \forall \beta = \left(\delta D_\eta, \delta D_\tau\right) \in \mathbb{R}^+ \times \mathbb{R}^+. \tag{45}$$

4.4. Derivation of the Euler–Lagrange equations

The variational inequality (45) must be exploited following the same procedure described in Timofeev et al. (2020), which will thus be omitted here. The results of such a procedure are the following two Euler–Lagrange equations,

$$\begin{cases} -k_\eta\left(1 - D_\eta\right) u_\eta - k_\tau B_\tau \dfrac{\partial \widetilde{B}_\tau}{\partial u_\eta} \displaystyle\int_0^{D_\tau} \left[\log\left(1 - x\right)\right]^2 dx + F_\eta^{ext} \\ \quad + K_p\left\{\left[\nabla\left(\nabla u_\eta\right)\right]\hat{c}\cdot\hat{c}\right\} \end{cases} \left(\delta u_\eta\right) = 0$$

$$\left\{-k_\tau\left(1 - D_\tau\right)\boldsymbol{u}_\tau + F_\tau^{ext}\right\}\left(\delta \boldsymbol{u}_\tau\right) = 0$$

where x is an internal integration variable that is used only to avoid to write the analytical form of the integral, together with the two Karush–Kuhn–Tucker (KKT) conditions for damage variables (already derived in Timofeev et al. (2020))

$$\left[\left(u_\eta\right)^2 - \Theta\left(u_\eta\right) B_t^2 \left(\log\left(1 - D_\eta\right)\right)^2 - \Theta\left(-u_\eta\right) B_c^2 \left[\tan\left(D_\eta\right)\right]^2\right]\Delta D_\eta = 0, \tag{46}$$

$$\left[\left(\boldsymbol{u}_\tau\right)^2 - \left[B_\tau\right]^2 \left(\log\left(1 - D_\tau\right)\right)^2\right]\Delta D_\tau = 0, \tag{47}$$

The two KKT conditions (46), (47) for irreversible descriptors can be arranged in a more compact form a

$$\left\{D_\eta - \tilde{D}_\eta(u_\eta)\right\}\Delta D_\eta = 0 \tag{48}$$

$$\left\{D_\tau - \tilde{D}_\tau(\boldsymbol{u}_\tau)\right\}\Delta D_\tau = 0 \tag{49}$$

where the auxiliary threshold functions $\tilde{D}_\eta(u_\eta)$ and $\tilde{D}_\tau(\boldsymbol{u}_\tau)$ have been defined as follows

$$\tilde{D}_\eta(u_\eta) = \begin{cases} 1 - \exp\left(-\dfrac{u_\eta}{B_\eta^t}\right), & u_\eta > 0, \\ \dfrac{2}{\pi}\arctan\left(-\dfrac{u_\eta}{B_\eta^c}\right), & u_\eta < 0, \end{cases} \tag{50}$$

$$\tilde{D}_\tau(\boldsymbol{u}_\tau) = 1 - \exp\left(-\frac{\left|\boldsymbol{u}_\tau\right|}{B_\tau}\right), \tag{51}$$

5. Numerical results

5.1. Description of the numerical experiments

In the current section, we present numerical simulations to show the capabilities of the derived model to describe initiation and growth of damage localization zones. Following Timofeev et al. (2020) we consider 2D square specimen with a circular flaw (hole). Here $S = 10$ cm is the size of the sample and $R_h = 0.12 \cdot S$ is the hole's radius. In this work, two types of numerical experiments are employed:

1. In type 1, the specimen is subjected to tensile loading to demonstrate the effects of pantographic mechanism on the evolution and thickness of damage localization from the circular flaw. Fig. 5 (left) illustrates this loading type where we have imposed displacement $\bar{u}$ which is increasing monotonically during the tests within the range $[0, \bar{u}_{max}]$on the right-hand vertical boundary. Two cases of simulations are performed. One in which the averaged intergranular distance L is kept unchanged while the pantographic coefficient K_P is changed resulting in a change in the overall stiffness/strength of the specimen. And the second, in which the inter-granular stiffness are re-scaled for different averaged intergranular distance L, such that the overall stiffness/strength of the specimen remains unchanged while both the averaged intergranular distance L and the pantographic coefficient K_P are varied.
2. In type 2, the specimen is subjected to a more complex loading path by sequentially applying tensile and shear loading, as it is sketched in Fig. 5 (right), to demonstrate the effects of loading-path on the evolution and thickness of damage localization from the circular flaw. For all of the four boundaries of the specimen we apply two conditions, i.e.

$$\begin{cases} u_1 &= \tilde{u}_1(x, y) = \bar{u}_1 \cdot (x/S) \\ u_2 &= \tilde{u}_2(x, y) = \bar{u}_2 \cdot (x/S) \end{cases} \quad \forall (x, y) \in [0, S] \times [0, S] \tag{52}$$

where u_1 and u_2 are horizontal and vertical components of the displacement field $\boldsymbol{u}$. Eq. (52) implies that the left-hand side of the sample is blocked both for horizontal u_1 and for vertical u_2 displacements

$$u_1 = \tilde{u}_1(0, y) = 0$$
$$u_2 = \tilde{u}_2(0, y) = 0$$

since $x = 0$ in this case, whereas on the right-hand side we have imposed displacements

$$u_1 = \tilde{u}_1(S, y) = \bar{u}_1$$
$$u_2 = \tilde{u}_2(S, y) = \bar{u}_2.$$

At the top as well as at the bottom imposed displacement for each point of the boundary increases with horizontal coordinate $x \in [0, S]$. Both horizontal and vertical imposed displacements are monotonically increasing within the ranges $[0, \bar{u}_1^{max}]$ and $[0, \bar{u}_2^{max}]$ respectively. We consider two cases of simulations to describe path-dependency of the system evolution for the derived model. One case in which the simulation starts with tensile

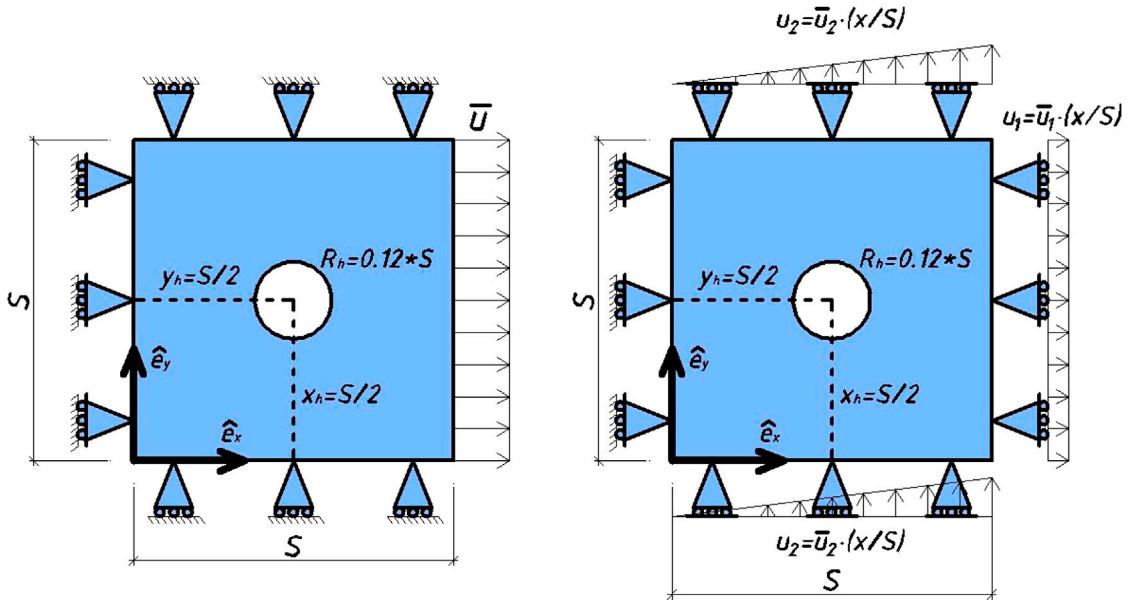

Fig. 5. Schematics of analyzed domains and considered boundary conditions.

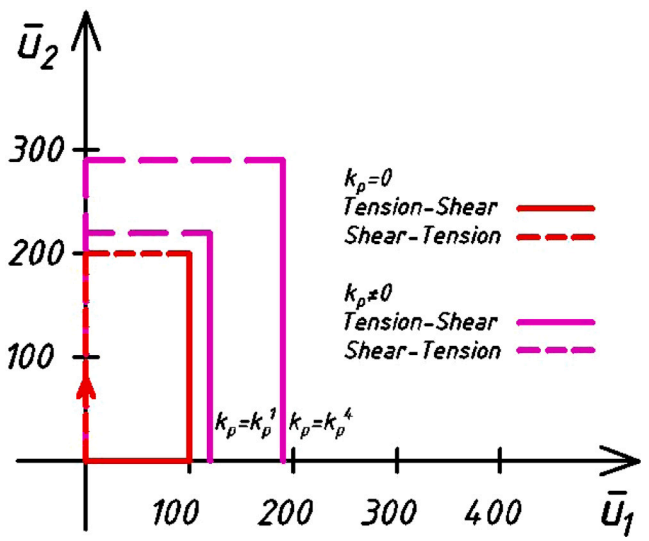

Fig. 6. Graphic representation of the loading path with respect to number of loading steps.

loading, increasing $\bar{u}_1$ while keeping $\bar{u}_2$ null, and then switch to shear loading, increasing $\bar{u}_2$ keeping $\bar{u}_1$ unchanged, such that the specimen in first subjected to tensile loading followed by shear loading. In the second case, we first apply shear loading and then switch to tensile loading, such that the final deformed external shape of the specimen remains the same. For both of these cases, we keep the averaged intergranular distance L unchanged while the pantographic coefficient K_P is changed resulting in a change in the overall stiffness/strength of the specimen. The loading paths for the two cases are represented graphically in Fig. 6 for pantographic coefficient $K_P = 0$, $K_P = K_P^1$ and $K_P = K_P^4$. In Fig. 6, the axis refer to the number of loading steps highlighted later in the Table 4.

5.2. Re-scaling with the averaged intergranular distance

In this Sub-section we consider a class of materials with the same stiffness and damage characteristics but different averaged intergranular distance L. To do this, we introduce a re-scaling parameter $\gamma \in \mathbb{R}^+$ for changing the averaged intergranular distance from L to L^* as follows:

$$L^* = \frac{L}{\gamma}. \tag{53}$$

Such re-scaling should therefore correspond to materials with similar elastic and damage behavior. Thus, in particular the consequence is (i) an identical 4th rank elasticity tensor $\mathbb{C}^*$, i.e.,

$$\mathbb{C}^* = \mathbb{C}$$

and from Eq. (30) we deduce the following re-scaling rule for intergranular stiffness,

$$\begin{cases} \left(k_\eta^t\right)^* (L^*)^2 = k_\eta^t L^2 \\ \left(k_\eta^c\right)^* (L^*)^2 = k_\eta^c L^2 \\ \left(k_\tau\right)^* (L^*)^2 = k_\tau L^2, \end{cases} \rightarrow \begin{cases} \left(k_\eta^t\right)^* = \gamma^2 k_\eta^t \\ \left(k_\eta^c\right)^* = \gamma^2 k_\eta^c \\ k_\tau^* = \gamma^2 k_\tau, \end{cases} \tag{54}$$

and (ii) similar damage characteristic lengths. To do this we recall the expressions of the auxiliary threshold functions in Eqs. (50), (51) and consider

$$\begin{cases} \frac{u_\eta^*}{(B_\eta^c)^*} = \frac{u_\eta}{B_\eta^c} \\ \frac{u_\eta^*}{(B_\eta^t)^*} = \frac{u_\eta}{B_\eta^t} \\ \frac{|u_\tau^*|}{B_\tau^*} = \frac{|u_\tau|}{B_\tau}, \end{cases} \rightarrow \begin{cases} \left(B_\eta^t\right)^* = \frac{B_\eta^t}{\gamma} \\ \left(B_\eta^c\right)^* = \frac{B_\eta^c}{\gamma} \\ B_{\tau 0}^* = \frac{B_{\tau 0}}{\gamma}, \end{cases} \tag{55}$$

where the definitions (12) and (14) of normal and tangent displacement have been used to deduce the following approximations for their order of magnitudes,

$$u_A^* \cong \frac{L^*}{L} u_A = \frac{u_A}{\gamma}, \quad A = \eta, \tau. \tag{56}$$

For the same reason and taking into account Eq. (20), the regularizing parameter α, the one used to smooth the constitutive assumption on

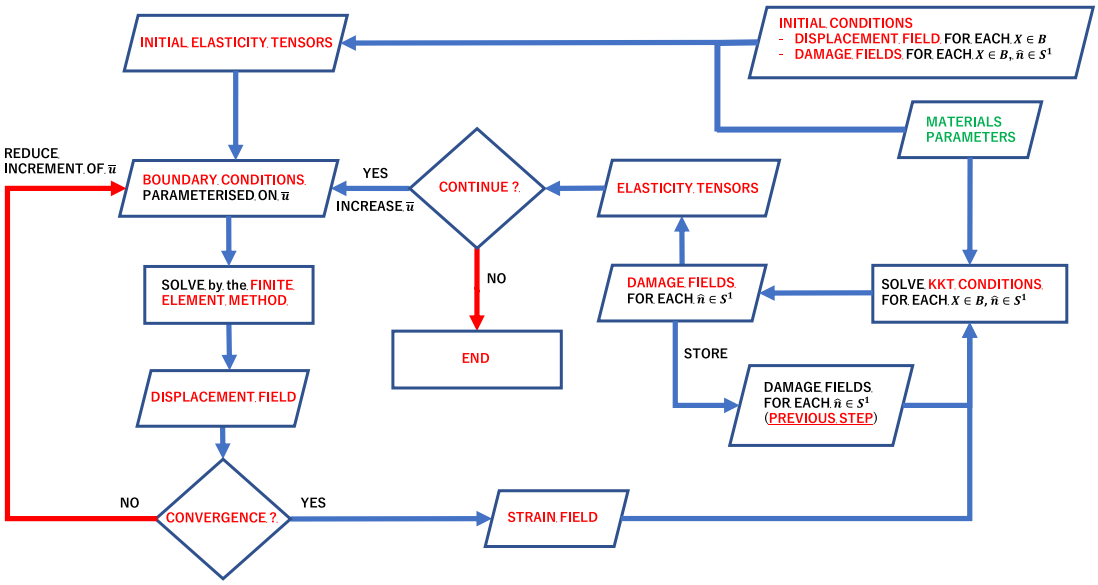

Fig. 7. Flowchart of the numerical iterative procedure used to solve the mathematical formulation.

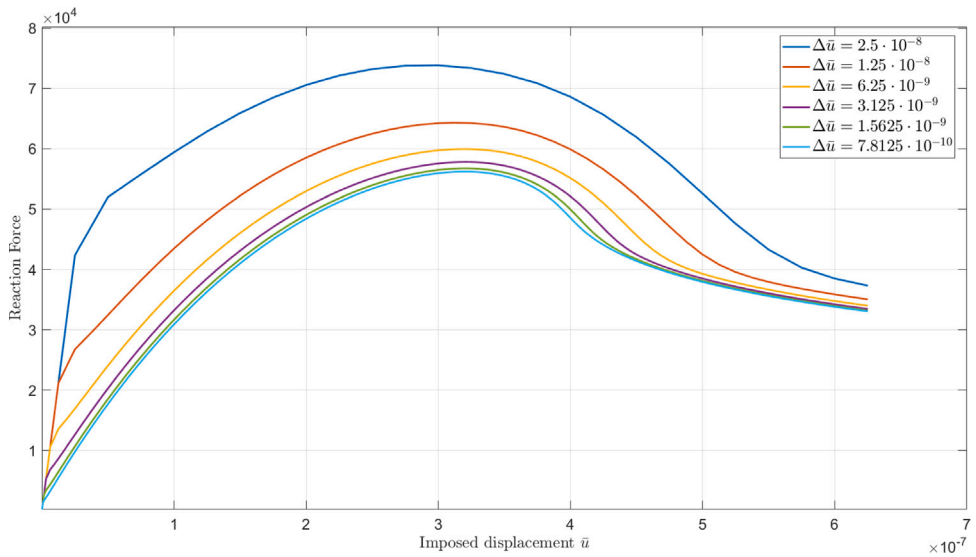

Fig. 8. Convergence analysis with respect to the size of the load step $\Delta\bar{u}$. Global elastic response, i.e. total reaction force vs prescribed displacement for the pantographic coefficient $K_P = K_P^3$.

tension–compression asymmetry in Eq. (21), for the sake of numerical accuracy has been re-scaled as follows,

$$\frac{u_\eta^*}{\alpha^*} = \frac{u_\eta}{\alpha}, \quad \rightarrow \quad \alpha^* = \frac{\alpha}{\gamma}. \tag{57}$$

It is worth to be noted that, as a consequence of the re-scalings assumed in (53), (54), (55) and (57) on the one hand the 5th rank elasticity tensor $\mathbb{M}$ will be re-scaled as follows

$$\mathbb{M}^* = \frac{(L^*)^3}{L^3}\frac{\left(k_\eta^t\right)^*}{k_\eta^t}\mathbb{M} = \frac{1}{\gamma^3}\gamma^2\mathbb{M} = \frac{\mathbb{M}}{\gamma}, \tag{58}$$

and, on the other hand, in order to derive the re-scaling rule for the 6th rank elasticity tensor $\mathbb{D}$, we need to prescribe a re-scaling rule also for the pantographic coefficient K_P. To do this we consider first the case of no pantographic coefficient and derive,

$$K_P = 0, \quad \rightarrow \quad \mathbb{D}^* = \frac{(L^*)^4}{L^4}\frac{\left(k_\eta^t\right)^*}{k_\eta^t}\mathbb{D} = \frac{1}{\gamma^4}\gamma^2\mathbb{D} = \frac{\mathbb{D}}{\gamma^2}. \tag{59}$$

In this case we remark that in the limit of zero averaged intergranular distance $L \rightarrow 0$ (i.e. from (53) in the limit $\gamma \rightarrow \infty$) we derive, from (58) and (59), that $\mathbb{M}^* \rightarrow \mathbf{0}$ and $\mathbb{D}^* \rightarrow \mathbf{0}$, i.e. a situation with no strain gradient effects and therefore vanishingly thin boundary layers in the numerical simulations. However, the presence of the pantographic term changes this undesired effect by ensuring that in this limit the 6th rank elasticity tensor may be the same, i.e.,

$$\lim_{\gamma\rightarrow\infty} \mathbb{D}^* = \mathbb{D} \quad \rightarrow \quad \left(L^*\right)^2 K_P^* = L^2 K_P \quad \rightarrow \quad K_P^* = \gamma^2 K_P,$$

that is, by employing the same re-scaling rules as that for the other stiffness coefficients given in (54).

5.3. Constitutive coefficients setting

For illustration, we will consider three sets of material parameters, namely the sets $\mathcal{P}_1$, $\mathcal{P}_2$ and $\mathcal{P}_3$ that are defined respectively by assuming $\gamma = 1$, $\gamma = 2$ and $\gamma = 5$ according to Tables 1–2, such as to consider a wide range of intergranular distance.

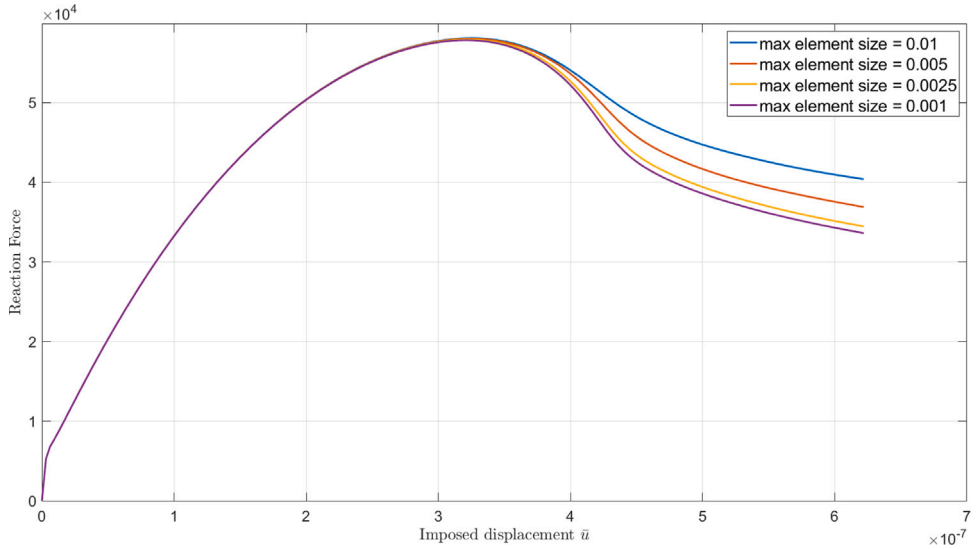

Fig. 9. Mesh-convergence analysis. Global elastic response, i.e. total reaction force vs prescribed displacement for the pantographic coefficient $K_P = K_P^3$.

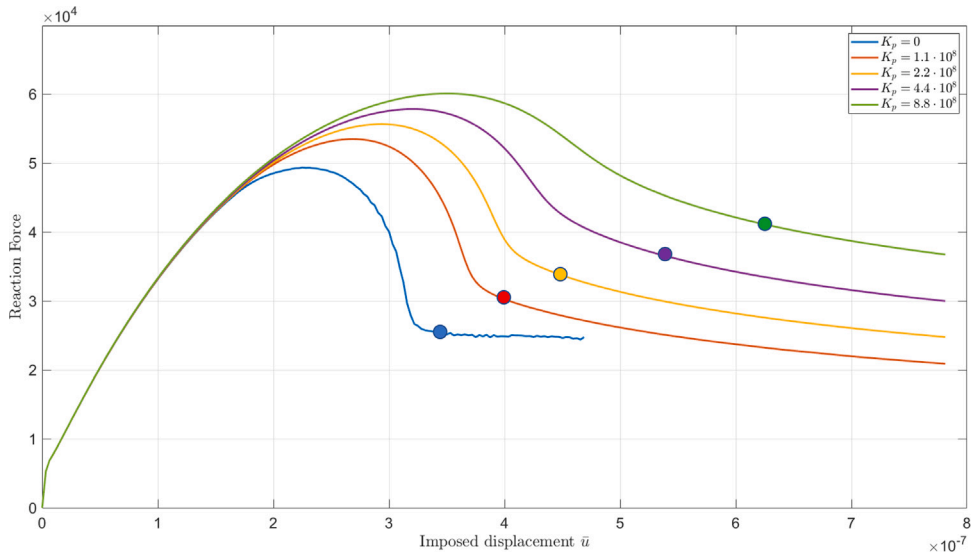

Fig. 10. Force versus displacement diagram for the $\mathcal{P}_1$ set of parameters defined in Tables 1–2 and for different values of K_P. Circle markers indicate approximately the time step, when the crack reaches the boundary of the sample.

Table 1
Values of constitutive parameters used in numerical tests.

	γ	L [m]	k_η^c [J/m^4]	k_η^t [J/m^4]	k_τ [J/m^4]	B_η^c [m]	B_η^t [m]	B_τ [m]	α_1[1]	α_2[1]	α[1]
$\mathcal{P}_1$	1	0.01	$1.4 \cdot 10^{15}$	$1.4 \cdot 10^{14}$	$3 \cdot 10^{13}$	$1.5 \cdot 10^{-7}$	$3.5 \cdot 10^{-8}$	$5 \cdot 10^{-8}$			$3 \cdot 10^{-10}$
$\mathcal{P}_2$	2	0.005	$5.6 \cdot 10^{15}$	$5.6 \cdot 10^{14}$	$1.2 \cdot 10^{14}$	$7.5 \cdot 10^{-8}$	$1.75 \cdot 10^{-8}$	$2.5 \cdot 10^{-8}$	10	14	$1.5 \cdot 10^{-10}$
$\mathcal{P}_3$	5	0.002	$35 \cdot 10^{15}$	$35 \cdot 10^{14}$	$7.5 \cdot 10^{14}$	$3 \cdot 10^{-8}$	$7 \cdot 10^{-9}$	$1 \cdot 10^{-8}$			$75 \cdot 10^{-11}$

Moreover, the values of the pantographic coefficients have been selected by comparing the first and the third row of (32) with the following rule,

$$K_P^i = k_\eta^t L^2 2^{i-8} \tag{60}$$

so that with $i = 4$ the first and the third row of (32) have the same order of magnitude, so that the pantographic coefficient and the tension stiffness have the same role and order of magnitude in the 6th rank elasticity tensor but with $i = 3$ the pantographic coefficient is the half, with $i = 2$ it is one fourth and with $i = 1$ is one eighth, such that the characteristic length of the boundary layers can also be independently varied (controlled).

Finally, for the simulation setups one can see Table 3.

Table 2
Values of the pantographic coefficient K_p used in numerical tests.

	γ	$K_P = 0$	K_P^1 [J/m^2]	K_P^2 [J/m^2]	K_P^3 [J/m^2]	K_P^4 [J/m^2]
$\mathcal{P}_1$	1	0	$1.1 \cdot 10^8$	$2.2 \cdot 10^8$	$4.4 \cdot 10^8$	$8.8 \cdot 10^8$
$\mathcal{P}_2$	2	0	$4.4 \cdot 10^8$	$8.8 \cdot 10^8$	$17.6 \cdot 10^8$	$35.2 \cdot 10^8$
$\mathcal{P}_3$	5	0	$27.5 \cdot 10^8$	$55 \cdot 10^8$	$11 \cdot 10^9$	$22 \cdot 10^9$

5.4. Implementation of the numerical algorithm

For the solution of the problem formulated above, numerical effort is needed. To this end, an algorithm was developed for the numerical

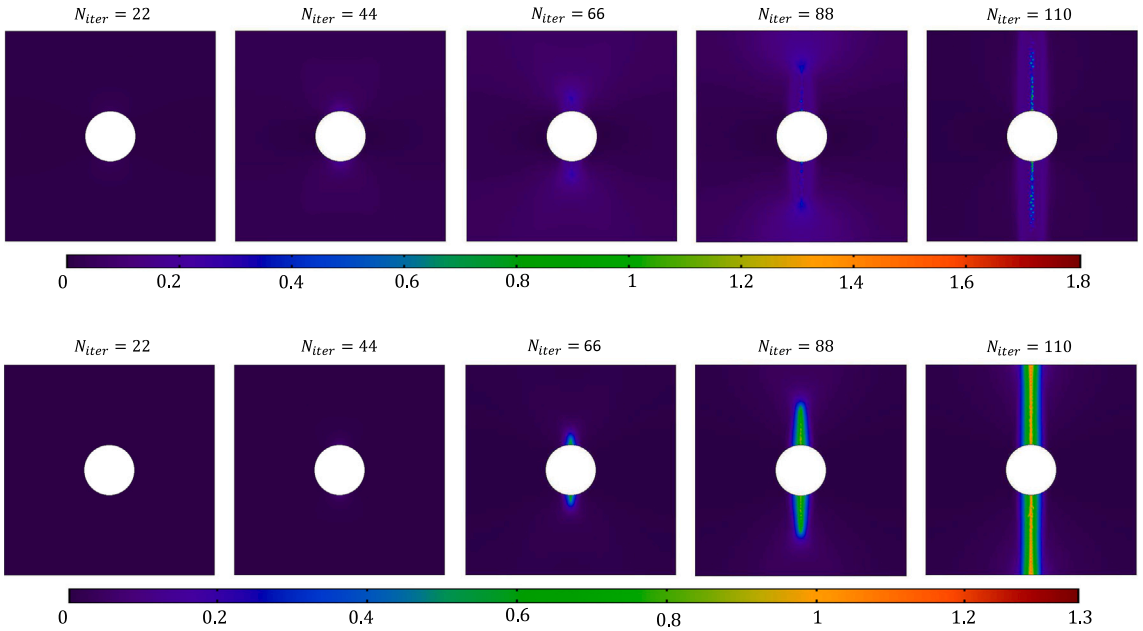

Fig. 11. Contour plots of elastic U (1st row) row) and dissipation W_D (2nd row) energy densities for $K_P = 0$ and for the $\mathcal{P}_1$ set of parameters defined in Tables 1–2.

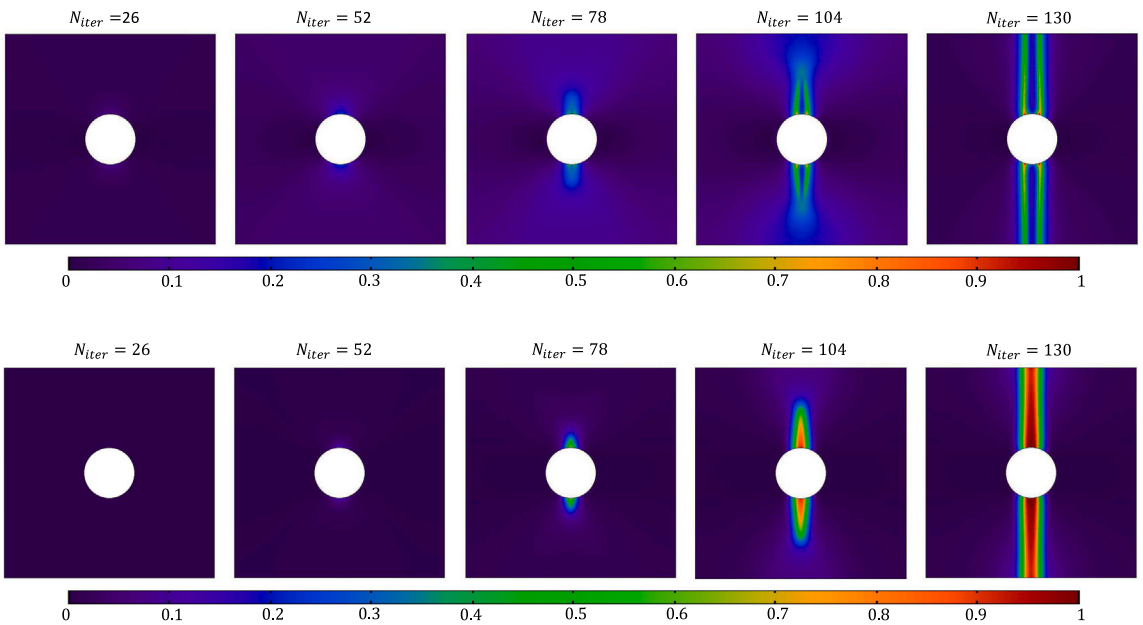

Fig. 12. Contour plots of elastic U (1st row) row) and dissipation W_D (2nd row) energy densities for $K_p = K_P^1 = 1.1 \cdot 10^8$ and for the $\mathcal{P}_1$ set of parameters defined in Tables 1–2.

Table 3
Numerical values used in numerical simulations.

N_θ	$\Delta\bar{u}$ [m]	$K_P = 0$		$K_P = K_P^i > 0$	
		N_{it}	$\bar{u}_{max}$ [m]	N_{it}	$\bar{u}_{max}$ [m]
120	$3.125 \cdot 10^{-9}$	150	$468.75 \cdot 10^{-9}$	250	$781.25 \cdot 10^{-9}$

implementation of the model. The continuum model is solved by means of the commercial software Matlab and COMSOL Multiphysics. An iterative procedure is implemented in a staggered fashion in Matlab as described in the flowchart in Fig. 7, making use of COMSOL Multiphysics as a subroutine solving the elastic equilibrium problem.

The steps of the iterative procedure can be resumed as follows:

1. null initial conditions on the displacement field $\boldsymbol{u}$ and damage fields D_η and D_τ are given together with the material parameters $L, k_\eta^c, k_\eta^t, k_\tau, B_\eta^c, B_\eta^t, B_{\tau 0}, K_P$, according to Tables 1–2. The stiffnesses $k_\eta^c, k_\eta^t, k_\tau$ given as input material parameters may be initially isotropic, i.e. they do not need to depend on the orientation angle θ. It is worth to mention that the effective (i.e. damaged-) stiffnesses $k_{\eta,D}^c, k_{\eta,D}^t, k_{\tau,D}$ may change during the evolution of the system due to the damage induced by the state of deformation, thus leading to non-isotropically distributed effective (damaged-) stiffnesses. Indeed, owing to Eq. (28), this is the reason why – for a given basis – the components of the elasticity tensors may change during the evolution of the system, possibly implying anisotropy shifts. The pantographic coefficient, on the contrary, does not experience damage;
2. the fourth-rank ($\mathbb{C}_{ijab}$), the fifth-rank ($\mathbb{M}_{ijabc}$) and the sixth-rank ($\mathbb{D}_{ijhabc}$) elasticity tensors are computed according to Eqs. (30),

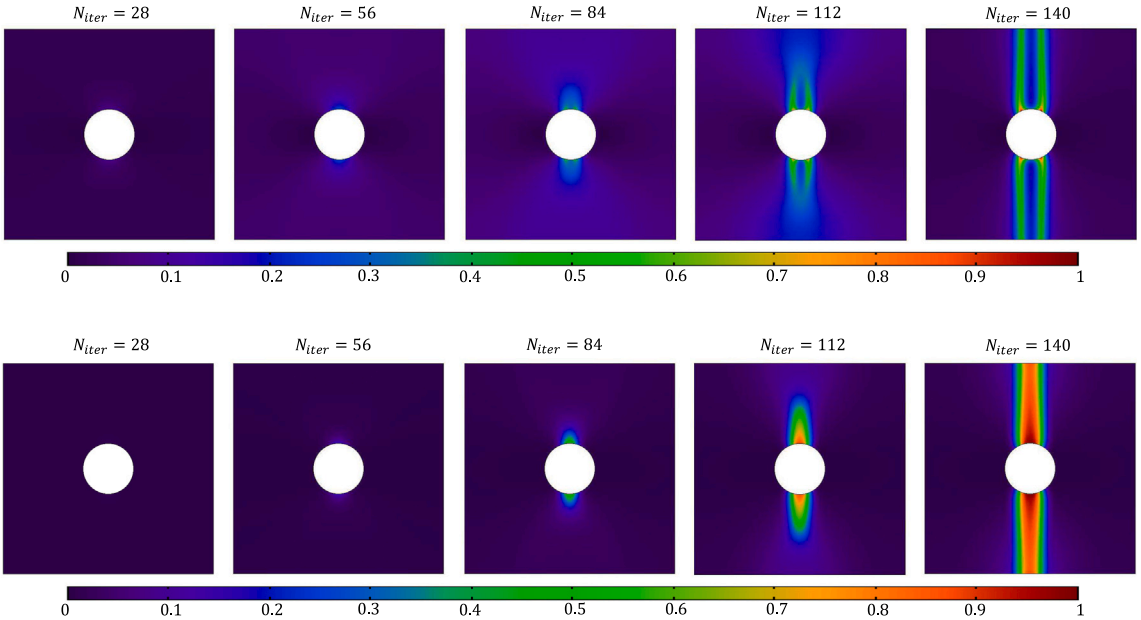

Fig. 13. Contour plots of elastic U (1st row) row) and dissipation W_D (2nd row) energy densities for $K_p = K_P^2 = 2.2 \cdot 10^8$ and for the $\mathcal{P}_1$ set of parameters defined in Tables 1–2.

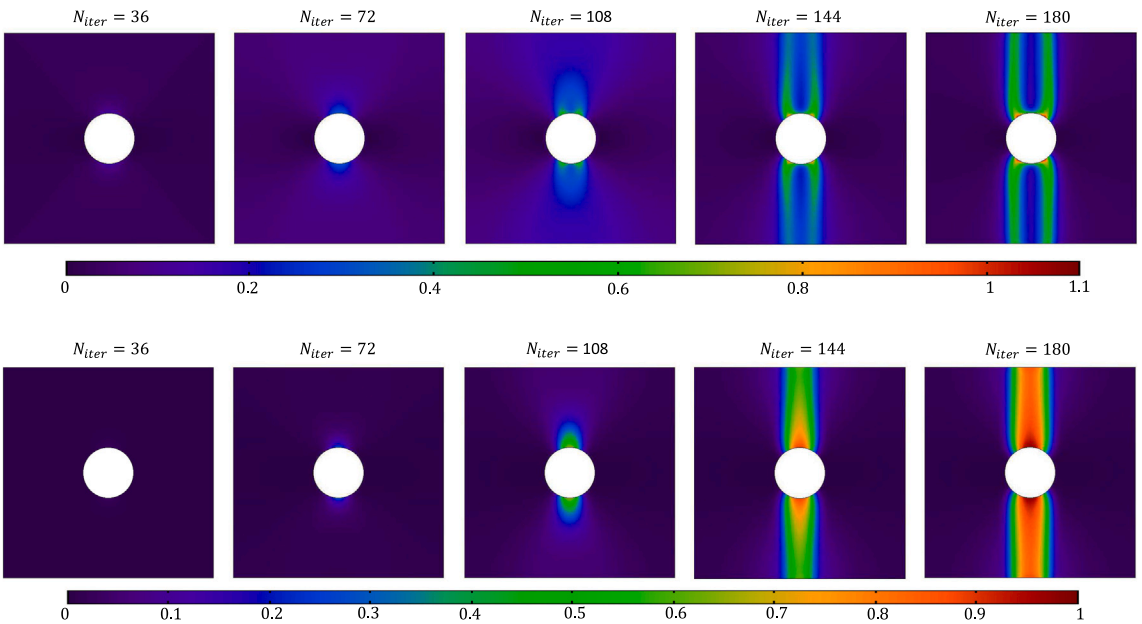

Fig. 14. Contour plots of elastic U (1st row) row) and dissipation W_D (2nd row) energy densities for $K_p = K_P^3 = 4.4 \cdot 10^8$ and for the $\mathcal{P}_1$ set of parameters defined in Tables 1–2.

(31) and (32). Such elastic tensors, as well as boundary conditions, are given as input to a finite element subroutine based on COMSOL Multiphysics. Particularly, the weak form of the equilibrium problem in Eq. (45) is solved by means of the *weak form* package. Quintic Argyris polynomials are used as shape functions ensuring C^2 continuity across elements along the normal to element boundaries. A Delaunay-tessellated triangular mesh was employed. Different mesh sizes were considered to investigate mesh independence. The output of this subroutine is the displacement field. It is worth to mention here that the pantographic coefficient K_p does not experience any change due to damage evolution;

3. the increment of the displacement field with respect to the previous step is node-wise compared with a tolerance. When such a tolerance is not respected, then the displacement parameters $\bar{u}$ or $\bar{u}_1$, $\bar{u}_2$ are reduced to re-initialize the finite element subroutine;
4. when the increment of the displacement field with respect to the previous step compares positively with the above-mentioned chosen tolerance, then the components of the strain field $\boldsymbol{G}$ and of its gradient are computed making use of the displacement field. The strain fields are then used by means of Eq. (11) to compute the relative displacements u_η and $\boldsymbol{u}_\tau$, which depend on the space coordinates and on the orientation θ. Such displacements are then given as input to the KKT conditions in Eqs. (50) and (51) and, as an output, the damage fields D_η and D_τ are recovered. In formulas, we have

$$D_\eta^t = \max\left\{\tilde{D}_\eta^t, D_\eta^{t-1}\right\}, \quad D_\tau^t = \max\left\{\tilde{D}_\tau^t, D_\tau^{t-1}\right\}, \tag{61}$$

where t is an index used to label the loading steps. Eqs. (61) have been conceived to take into account that, according to Eqs. (50) and (51), damage fields cannot decrease and they do not reach the unit value;

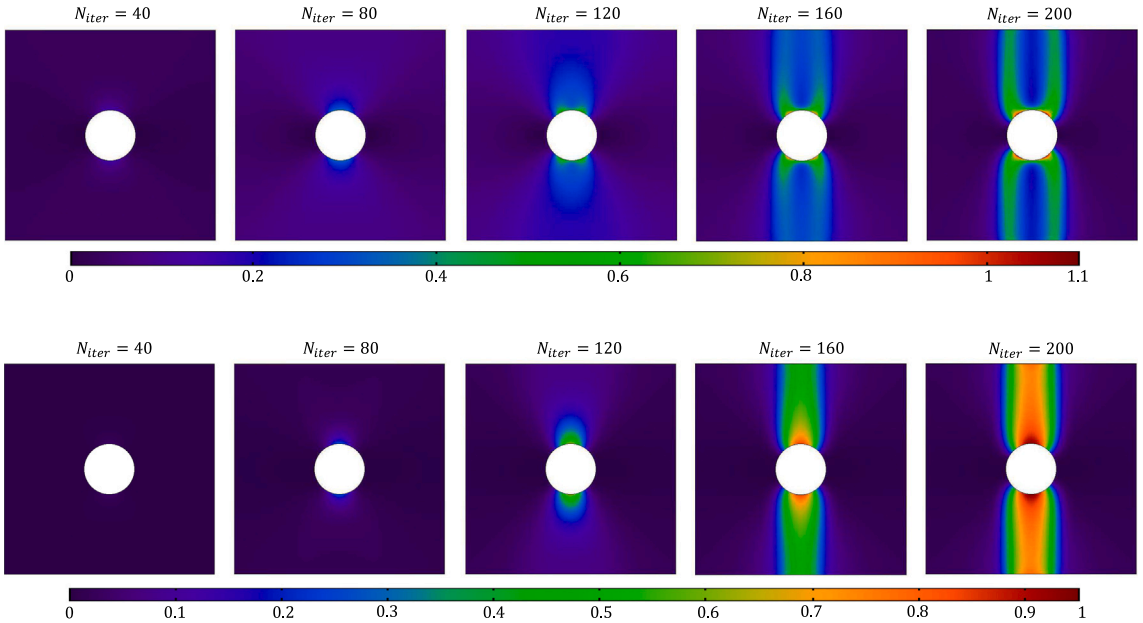

Fig. 15. Contour plots of elastic U (1st row) row) and dissipation W_D (2nd row) energy densities for $K_p = K_P^4 = 8.8 \cdot 10^8$ and for the $\mathcal{P}_1$ set of parameters defined in Tables 1–2.

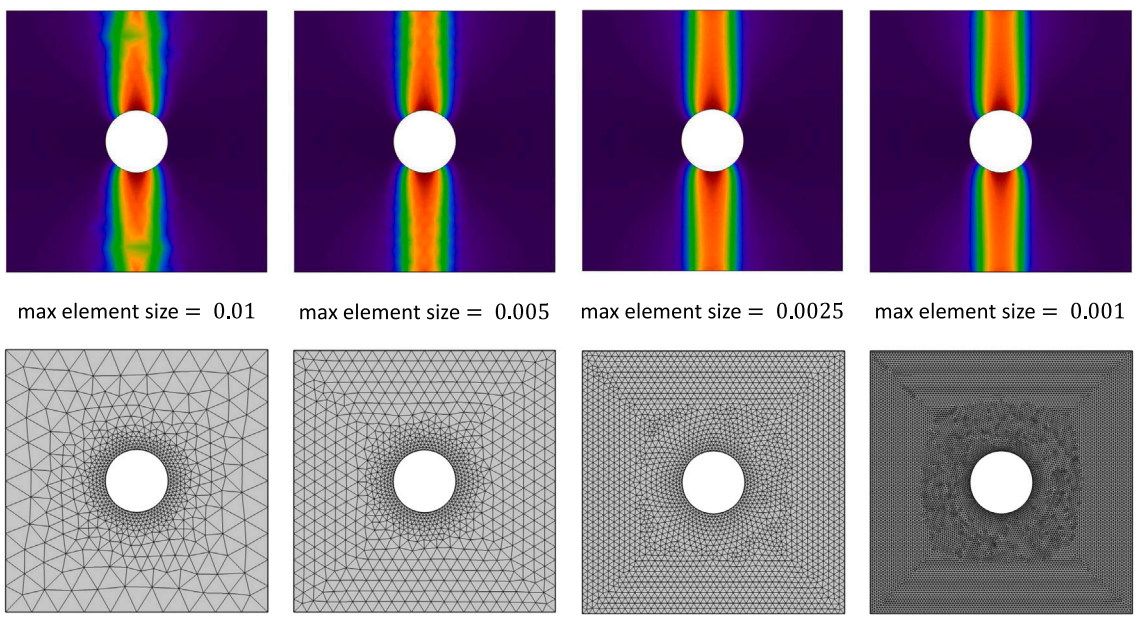

Fig. 16. Contour plots of dissipation energy density W_D (1st row) for $K_p = K_P^3 = 4.4 \cdot 10^8$ and for the $\mathcal{P}_1$ set of parameters defined in Tables 1–2 obtained for a given loading step $N_{it} = 180$ for different meshes (2nd row).

5. the load parameter $\bar{u}$ is increased.

The instructions above (from point 2) are repeated until a termination criterion is not verified. As mentioned at the beginning of the section, the termination criterion is given by $\bar{u}$ reaching a maximum desired value $\bar{u}_{max}$ or by reaching $\bar{u}_1$, $\bar{u}_2$ maximum values $\bar{u}_1^{max}$, $\bar{u}_2^{max}$ respectively.

5.5. Parametric analysis with respect to the pantographic coefficient for constant intergranular distance

In this subsection we consider results, according to Tables 1–2, of the $\mathcal{P}_1$ series of extension tests corresponding to the intergranular distance $L = 0.01$. The aim of performing these tests was to investigate mechanical properties of the model taking into account the pantographic interaction, which is imposed by choosing values of K_P different from zero, according to (60).

For the numerical loading process, we first perform a convergence analysis for the incremental loading size. Fig. 8 presents a convergence analysis with respect to the size of the load step $\Delta\bar{u}$. It is observed that convergence is taking place. For the subsequent simulations, $\Delta\bar{u} = 3.125 \cdot 10^{-9}$ is chosen, since the difference between the force displacement curve corresponding to this value of $\Delta\bar{u}$ and that related to the smallest $\Delta\bar{u}$ indicated in Fig. 8 is reasonably small, considering that for the smallest $\Delta\bar{u}$ it takes much more computational time to get results.

Fig. 9 shows that convergence with respect to the maximum mesh element size is taking place as well. For the subsequent simulations maximum element size equal to 0.001 is chosen.

In Fig. 10 one can see the computed force–displacement diagrams. It is clear from the plot that, by introducing K_P different from zero,

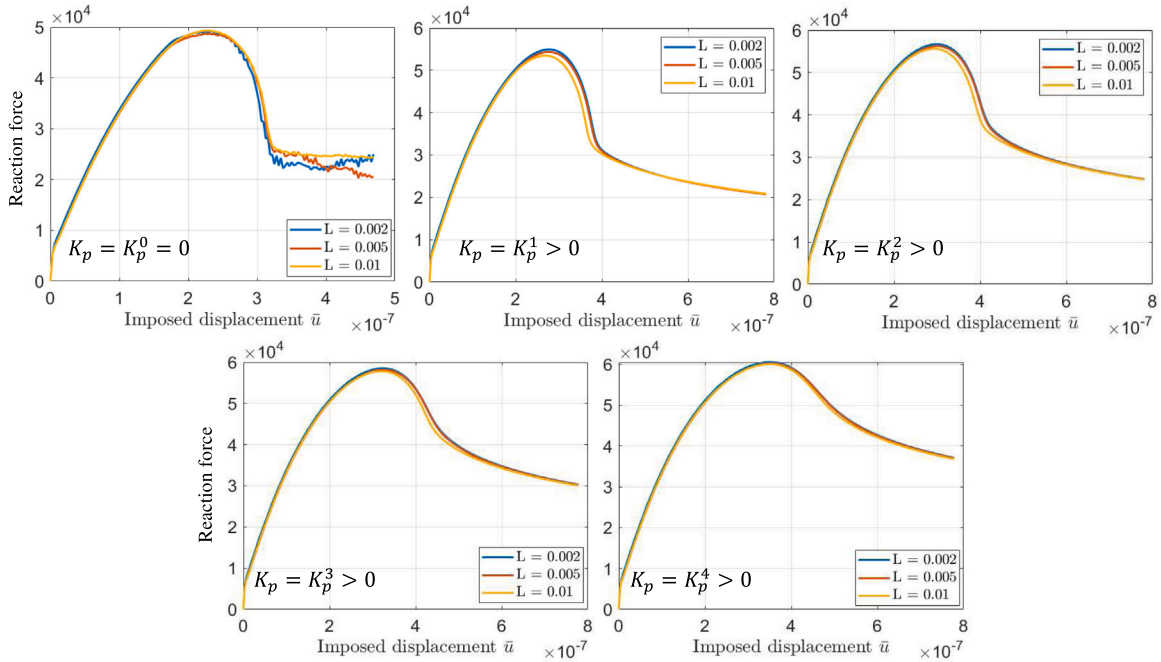

Fig. 17. Force versus displacement diagrams for different values of L and K_p.

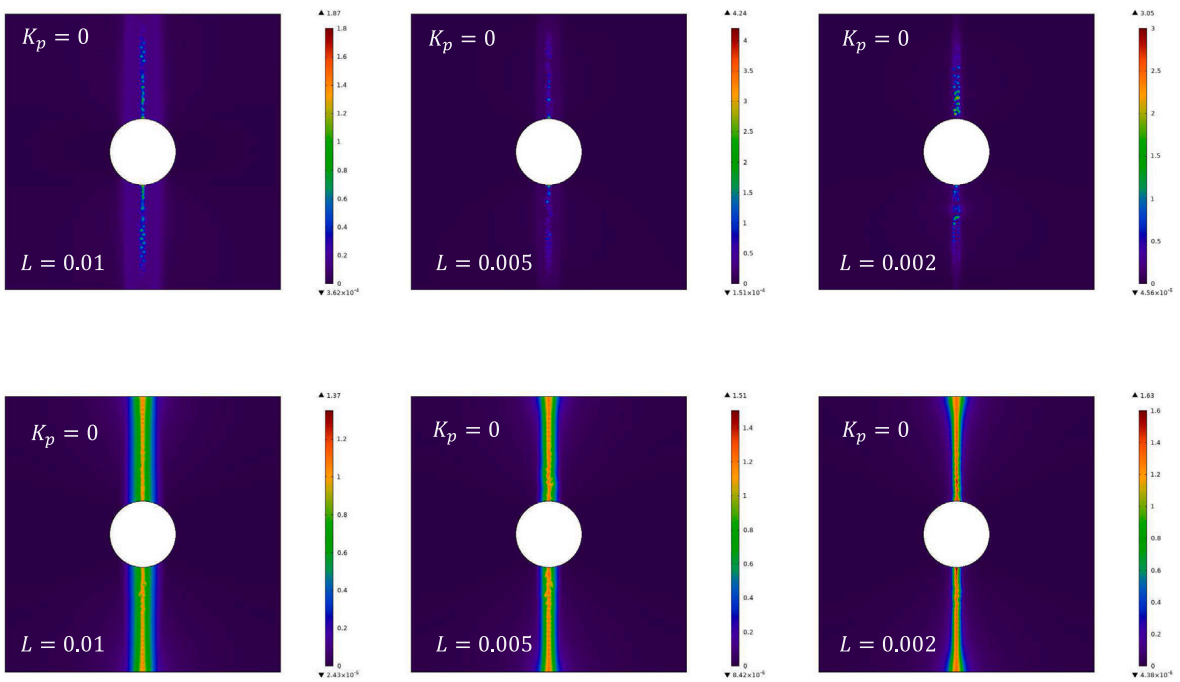

Fig. 18. Contour plots, at the final step, of elastic U (1st row) and dissipation W_D (2nd row) energy densities for $K_p = K_p^0$ and different L. All material parameters are rescaled in order to obtain the same Young modulus and Poissons ration for the calculations.

we obtain a stronger response of the sample with respect to the case of $K_P = 0$, as shown by the increase in peak reaction. Furthermore, increasing pantographic coefficient leads to an increase of the reaction force in the softening part of the response and a slowed rate of softening. The observed nature of the force–displacement curves can be exed by considering Eqs. (30)–(32), where expressions of elasticity tensors are presented. Specifically, the additional term K_P increases the values of the components of $\mathbb{D}$, and since K_P is not affected by damage, the components of $\mathbb{D}$ never vanish. Therefore, there will be always some elastic energy that is stored at each material point of the considered sample even as the damage within materials points tend to 1.

Figs. 11–15 show contour plots for elastic (1st row of contour plots) and dissipation (2nd row of contour plots) energy densities evolution throughout the simulation, where increasing N_{iter} indicates the increase in the imposed displacement. These contour plots show the development of concentration zones which emanate from the hole and grow towards the outer edges of the square specimen. The evolution of dissipation (due to damage in this case) is of particular interest in these simulations from the viewpoint of describing its localization as well as the characteristic length of the damage localization zone. These plots makes evident micro-mechanical effect of the pantographic interaction on the damage behavior on macro-scale. We can observe

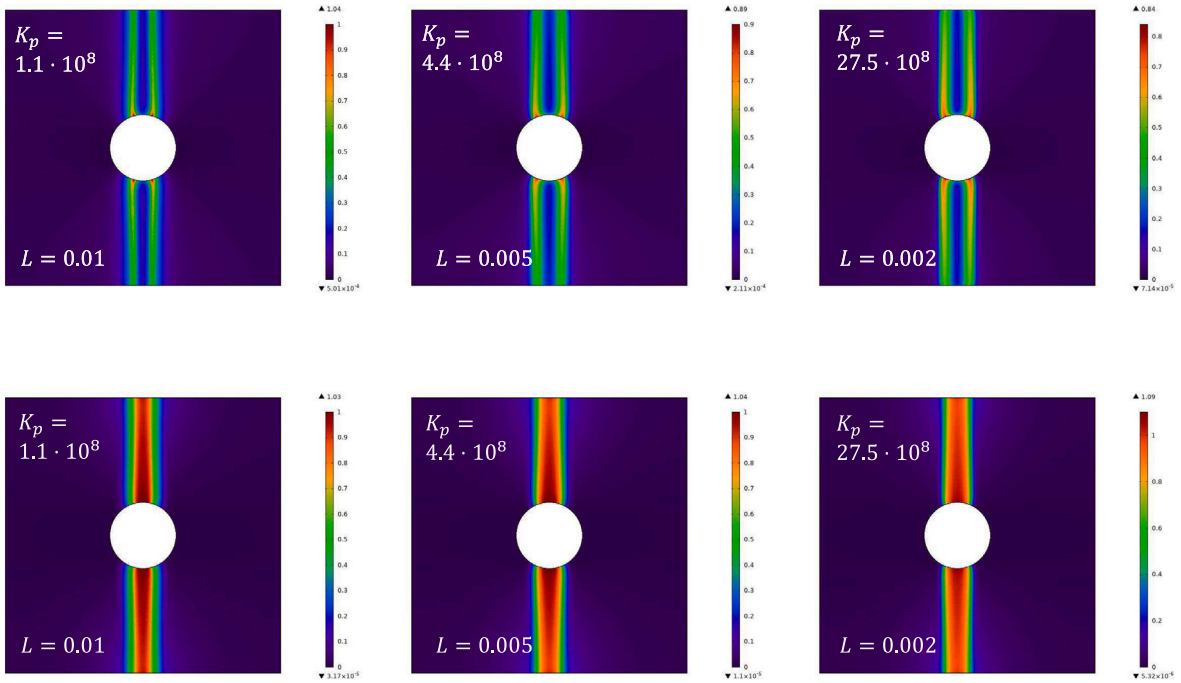

Fig. 19. Contour plots, at the final step, of elastic U (1st row) and dissipation W_D (2nd row) energy densities for $K_p = K_p^1$ and different L. All material parameters are re-scaled in order to obtain the same Young modulus and Poissons ratio for the calculations.

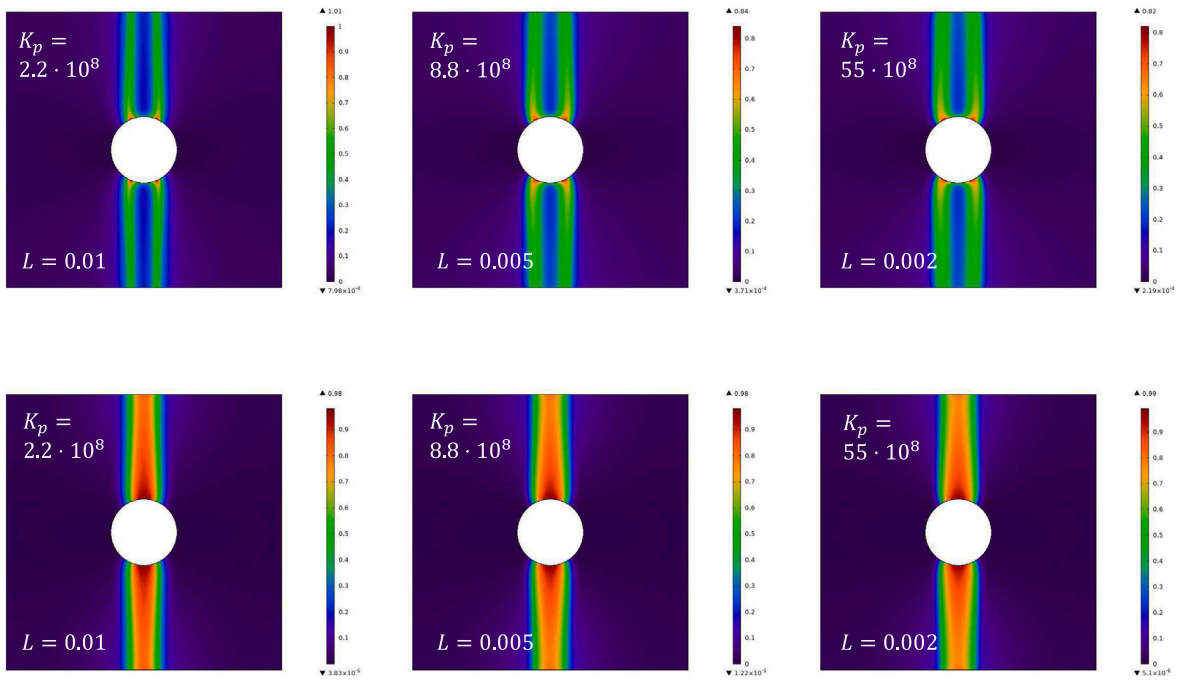

Fig. 20. Contour plots, at the final step, of elastic$U$ (1st row) and dissipation W_D (2nd row) energy densities for $K_p = K_p^2$ and different L. All material parameters (including K_p) are re-scaled in order to obtain the same Young modulus and Poissons ratio for the calculations.

that by choosing different pantographic coefficient, K_P, the width of the localization zone can be controlled. Indeed, a higher value of the pantographic coefficient, K_P, results in a thicker damage zone. We further note here that in the next section, the micromechanical effects are further illustrated by showing that model can predict localization zones that are independent of the intergranular distance, an effect which is a direct consequence of the pantographic interaction. The localization thickness could be described as proportional to the material characteristic length roughly estimated from the ratio of the 2nd and 1st gradient moduli in Eqs. (30)–(32), with the caveat that these moduli, and therefore, the characteristic lengths evolve during the loading process. For the case of pantographic coefficient, $K_P = 0$, the damage zone is thin as in this case it has the order of the averaged intergranular distance L. By selecting appropriate pantographic coefficient, K_P, the size of the localization zone can be increased in a pre-specified manner even to the order of the flaw size (in this case size of the circular hole), while keeping the averaged intergranular distance L unchanged. It is noteworthy, that the included pantographic effect can arise at

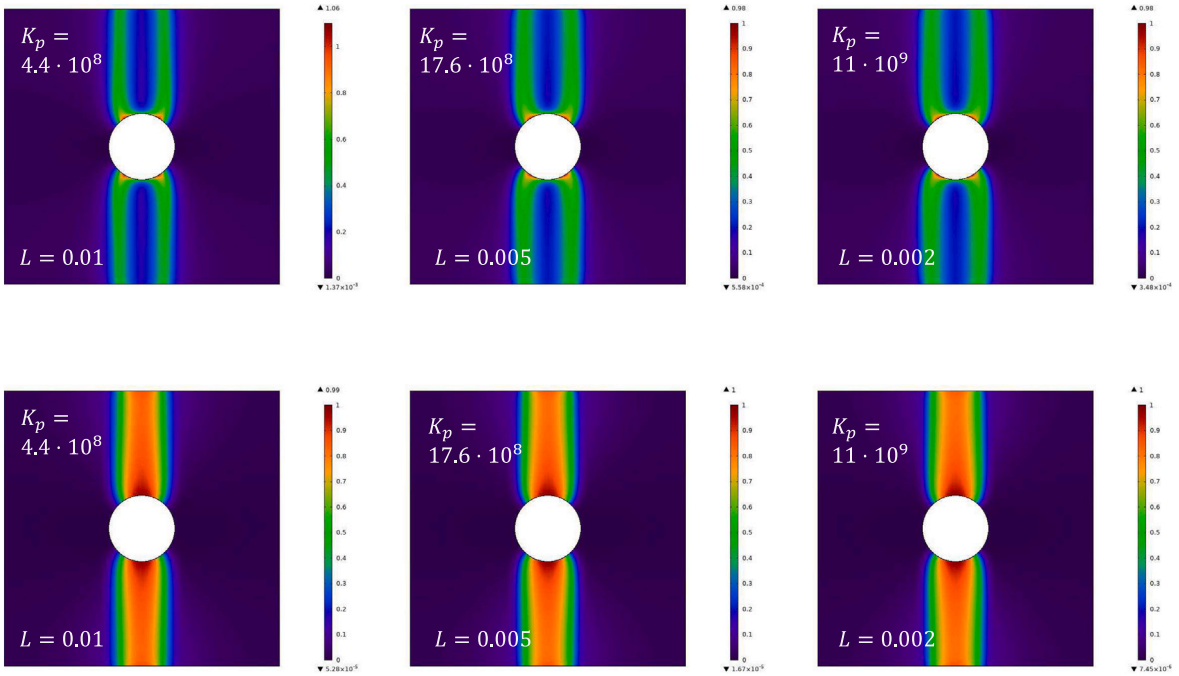

Fig. 21. Contour plots, at final step, of elastic U (1st row) and dissipation W_D (2nd row) energy densities for $K_p = K_p^3$ and different L. All material parameters (including K_p) are re-scaled in order to obtain the same Young modulus and Poissons ratio for the calculations.

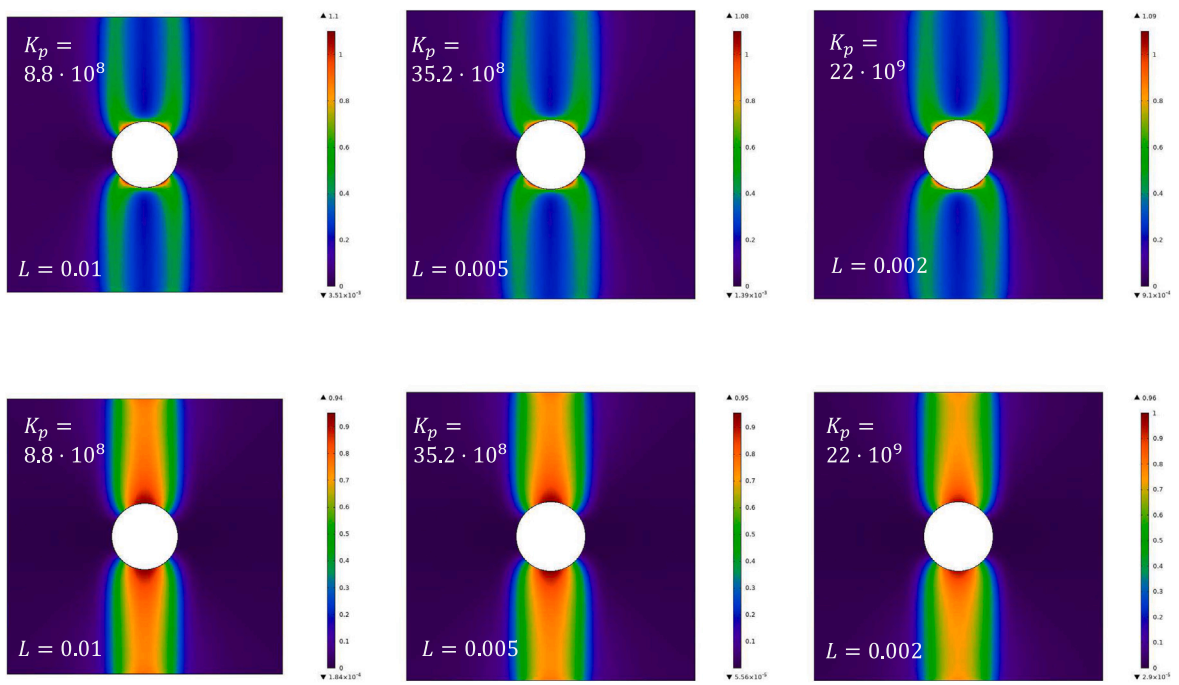

Fig. 22. Contour plots, at the final step, of elastic U (1st row) and dissipation W_D (2nd row) energy densities for $K_p = K_p^4$ and different L. All material parameters (including K_p) are re-scaled in order to obtain the same Young modulus and Poissons ratio for the calculations.

the micro- or grain-scale through a variety of long-range mechanisms, including grain rotation, that introduce floppy modes resulting from the micro-mechano-morphology of the material. Finally, it is worthwhile to note the concentration features in the elastic energy contours on the two edges of the damaged zone, which indicate the large elastic deformations that occur in the locations immediately contiguous to the damage localization.

Fig. 16 shows contour plots for dissipation energy (1st row of contour plots) with $K_P = K_P^2 = 2.2 \cdot 10^8$ for a given time step $N_{it} = 180$ and different meshes (2nd row of contour plots). It is observed, that thickness of the damaged area does not change with mesh refinement.

5.6. Parametric analysis for varying averaged intergranular distance

Fig. 17 shows 5 force–displacement diagrams, where each diagram is obtained for a given value of the pantographic coefficient $K_P = 0$ and $K_P = K_P^i$, $i = 1, \ldots, 4$ and for different set of parameters $\mathcal{P}_1$ ($\gamma = 1$), $\mathcal{P}_2$ ($\gamma = 2$) or $\mathcal{P}_3$ ($\gamma = 5$). The plots indicate that the re-scaling adopted

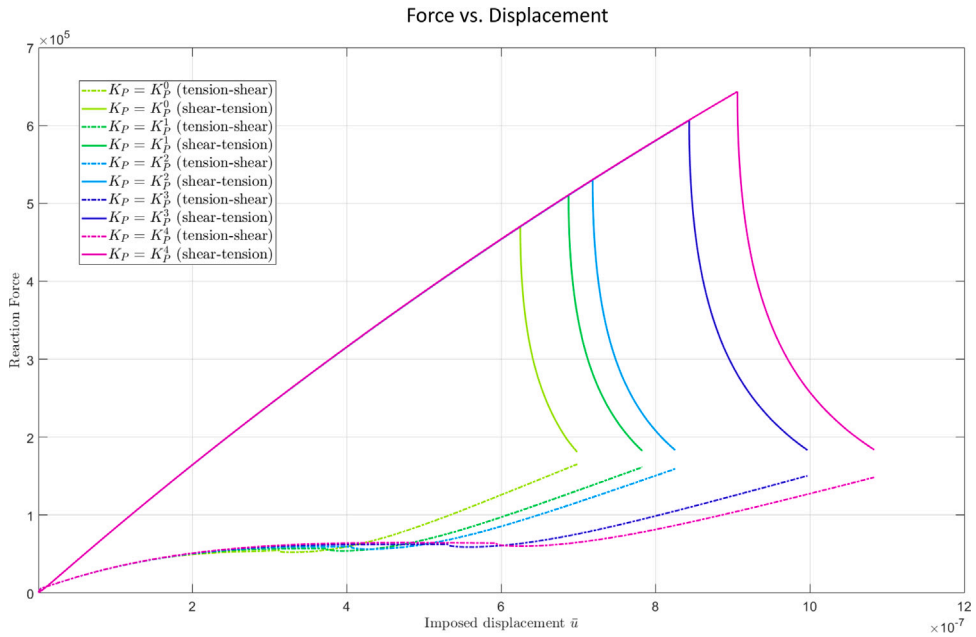

Fig. 23. Force versus displacement diagram for the $\mathcal{P}_1$ set of parameters defined in Tables 1–2 and for different values of K_P.

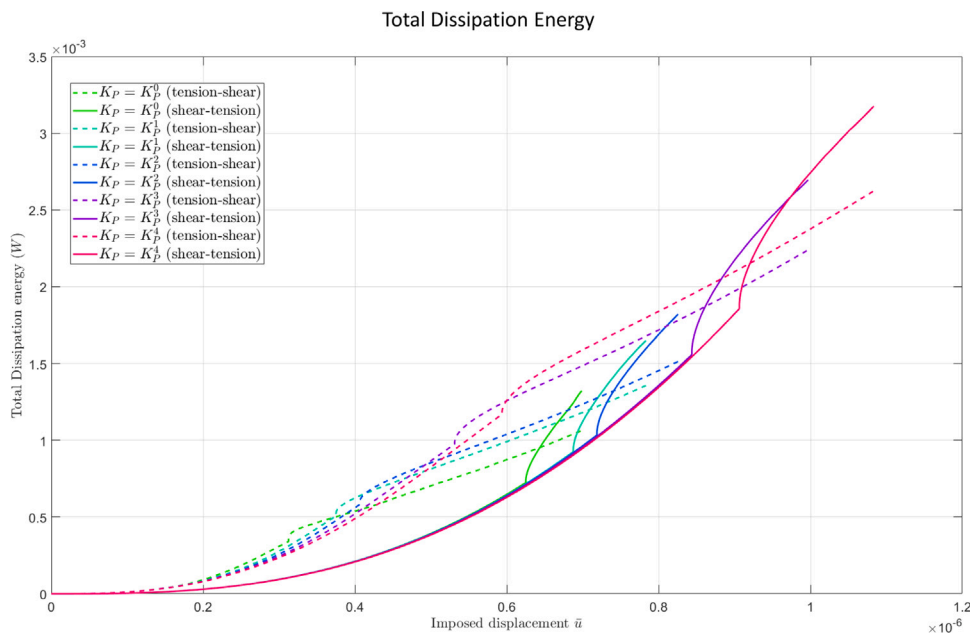

Fig. 24. Total dissipation energy versus displacement diagram for the $\mathcal{P}_1$ set of parameters defined in Tables 1–2 and for different values of K_P.

in Section 5.2 is valid because no significant difference is recognized for different values of γ and the higher is the pantographic coefficient K_P, the lower is such a difference.

Figs. 18–22 show contour plots for elastic (1st row of contour plots) and dissipation (2nd row of contour plots) energy densities at the final time step and for different sets of parameters $\mathcal{P}_1$ ($\gamma = 1$), $\mathcal{P}_2$ ($\gamma = 2$) or $\mathcal{P}_3$ ($\gamma = 5$) corresponding to different values of the intergranular distance L. It can be seen from the plots, that when $K_P = 0$ decreasing L implies also the reduction of the thickness of the damaged area, such that as the intergranular distance L, tends to vanish, the thickness of the localization zone will also vanish. Indeed, in most past micro-macro identification in which 2nd gradient stiffnesses are proportional to the square of the RVE or to the lattice size, or the intergranular distance L as it is here for $K_P = 0$, the 2nd gradient constants vanish in the limit of such a size going to zero. In these cases, the localization zone is restricted to be the size of the intergranular distance L.

However, for the cases $K_P = K_P^i > 0$, $i = 1, \dots, 4$ the situation is different. We can see that enhancing the pantographic interaction K_P means to attenuate such a reduction of the thickness of the damaged area. In other words, as the pantographic coefficient K_P increases, the thickness of the damage localization zone becomes independent of the intergranular distance L. In fact, through the proposed re-scaling, we define a family of discrete systems whose structural response remains invariant to change of grain size, but whose damage localization zone can be independently varied by accounting for the long-range effects modeled using the pantographic coefficient K_P. Hence, we may conjecture that physical systems obeying the discrete description could be designed such that second gradient effect remains non-negligible

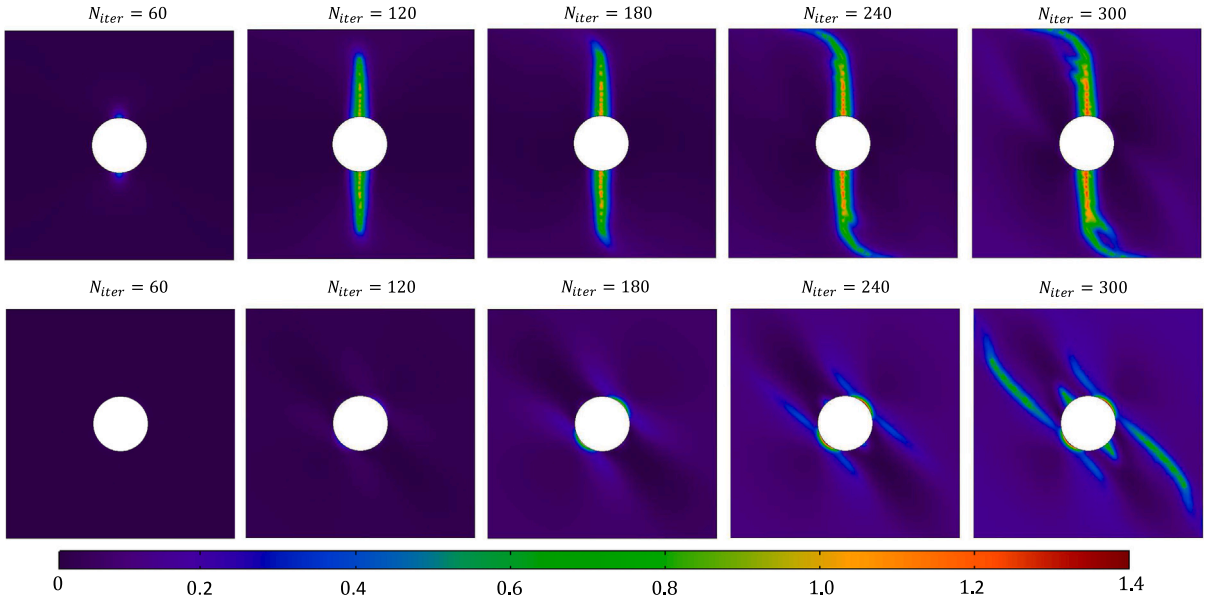

Fig. 25. Contour plots of dissipation W_D energy densities tension–shear (1st row) and shear–tension (2nd row) for $K_P = 0$ and for the $\mathcal{P}_1$ set of parameters defined in Tables 1–2.

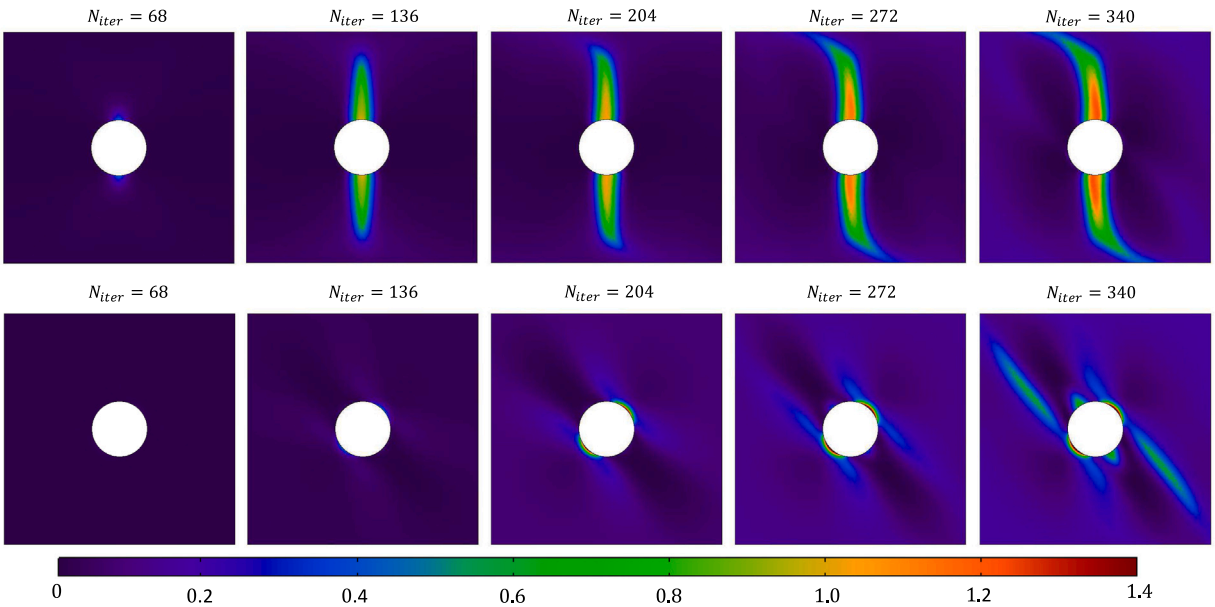

Fig. 26. Contour plots of dissipation W_D energy densities tension–shear (1st row) and shear–tension (2nd row) for $K_P = K_p^1$ and for the $\mathcal{P}_1$ set of parameters defined in Tables 1–2.

even for very dense physical systems. In this sense, embedding micro-structural interactions giving a non-zero gradient effect into an existing micro-structure could significantly improve the mechanical properties of the material.

5.7. Path-dependency of damage localization evolution

To further highlight the micromechanical effects on the macro damage model, we contrast the morphology of damage evolution under the tension–shear and shear–tension loading paths illustrated in Fig. 6. The details of the simulation steps for the two loading-paths are given in Table 4, where we note that the number of load-steps to reach a comparative damage condition increase with increasing K_P as seen from Fig. 10.

Further, in Fig. 23 we give the calculated reaction force–displacement response for the tension–shear and shear–tension simulations, where we consider the resultant reaction force and the imposed resultant displacement at the right vertical boundary. We can see, that the response for the tension–shear simulations is significantly different from the one for shear–tension simulations for each K_P. In particular, we can observe that the shear–tension response, which is dominated by the grain-scale shear interactions, are considerably

Table 4
Number of load-steps.

$K_P = K_p^0$	$N_{it}^{tens} = 100$	$N_{it}^{shear} = 200$	$N_{it}^{total} = 300$
$K_P = K_p^1$	$N_{it}^{tens} = 120$ (+20)	$N_{it}^{shear} = 220$ (+20)	$N_{it}^{total} = 340$
$K_P = K_p^2$	$N_{it}^{tens} = 130$ (+30)	$N_{it}^{shear} = 230$ (+30)	$N_{it}^{total} = 360$
$K_P = K_p^3$	$N_{it}^{tens} = 170$ (+70)	$N_{it}^{shear} = 270$ (+70)	$N_{it}^{total} = 440$
$K_P = K_p^4$	$N_{it}^{tens} = 190$ (+90)	$N_{it}^{shear} = 290$ (+90)	$N_{it}^{total} = 480$

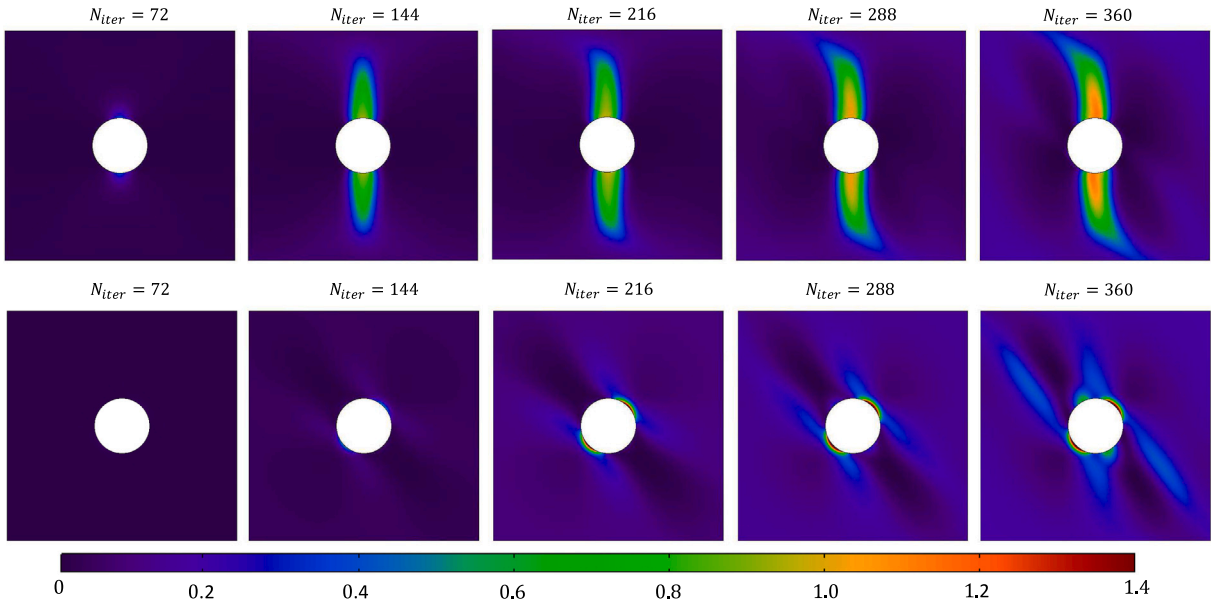

Fig. 27. Contour plots of dissipation W_D energy densities tension–shear (1st row) and shear–tension (2nd row) for $K_P = K_p^2$ and for the $\mathcal{P}_1$ set of parameters defined in Tables 1–2.

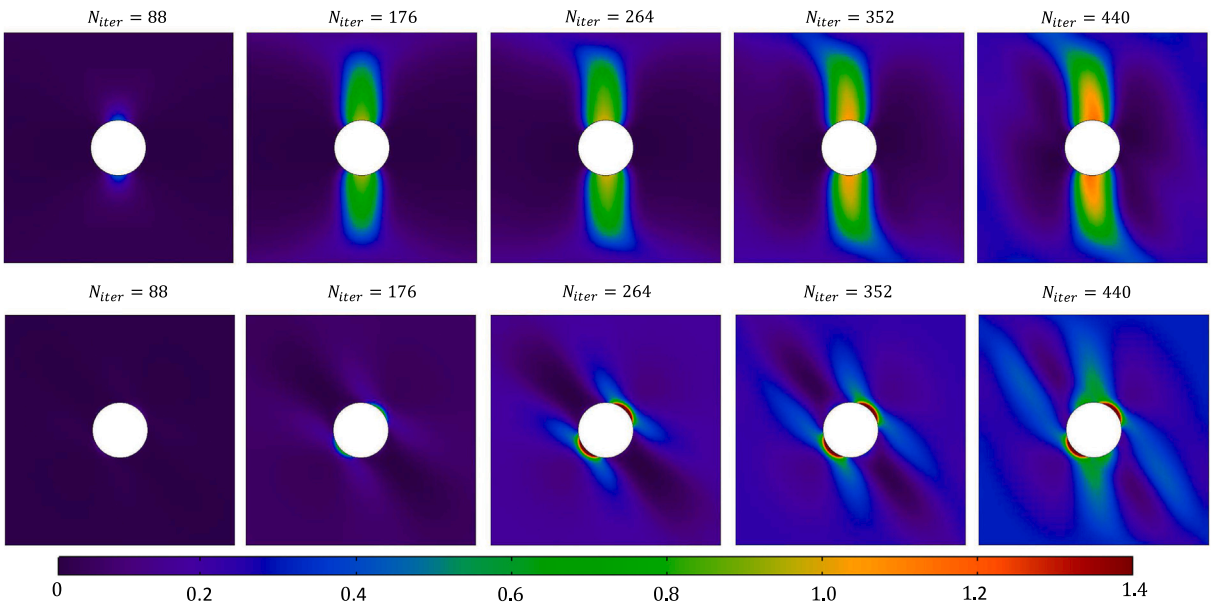

Fig. 28. Contour plots of dissipation W_D energy densities tension–shear (1st row) and shear–tension (2nd row) for $K_P = K_p^3$ and for the $\mathcal{P}_1$ set of parameters defined in Tables 1–2.

softer compared to the tension–shear response, dominated by the grain-scale normal interactions. The same conclusion can be made from Fig. 24 where total dissipation energy versus displacement diagram is presented. However, it is also interesting to observe that the final reaction, at the end of the loading, are close for both cases of simulations for each K_P. So although it appears that for a given deformed shape, the reaction force or dissipated energies are similar, the micromechanical effects predicate the loading path dependency of the force–displacement response during the loading process. This point is further illustrated by the evolution of the damage localization as shown in the Figs. 25–30 which show contour plots for dissipation energy densities evolution tension–shear (1st row of contour plots) and shear–tension (2nd row of contour plots) tests throughout the simulation for different K_P, where increasing N_{iter} indicates the increase in the imposed displacement. In the tension–shear test, we see that the damage zone progresses vertically, during the tensile phase, and subsequently tilts in the shear phase of the of loading path to form a winged zone. Furthermore, increasing K_P, results in controlling the thickness of the damage zone as well as in suppressing the emergence or manifestation of tilt. In contrast, in the shear–tension test we observe a completely different evolution of damage zone which develops in the diagonal direction under the shear phase and further grows diagonally under the tension phase. Although some rotation of the diagonal damage zone towards the vertical is notable whose extent is controlled by the pantographic coefficient K_P. It is clear from these simulation that the micro-macro correlations and the introduction of the pantographic coefficient K_P, introduce unprecedented load-path dependency that

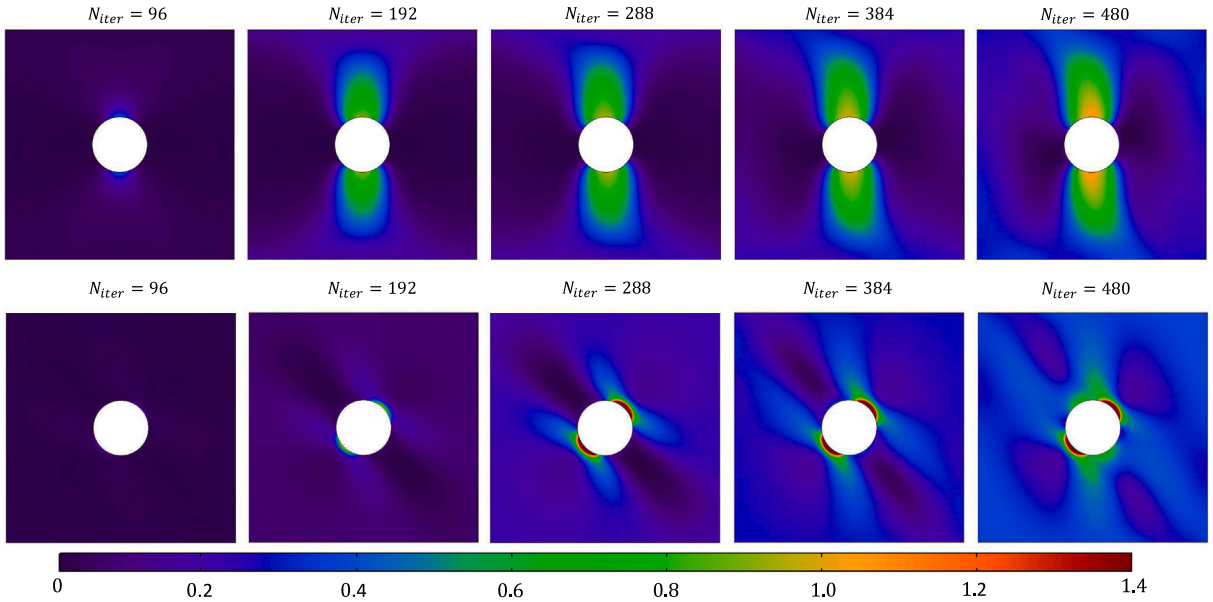

Fig. 29. Contour plots of dissipation W_D energy densities tension–shear (1st row) and shear–tension (2nd row) for $K_P = K_p^4$ and for the $\mathcal{P}_1$ set of parameters defined in Tables 1–2.

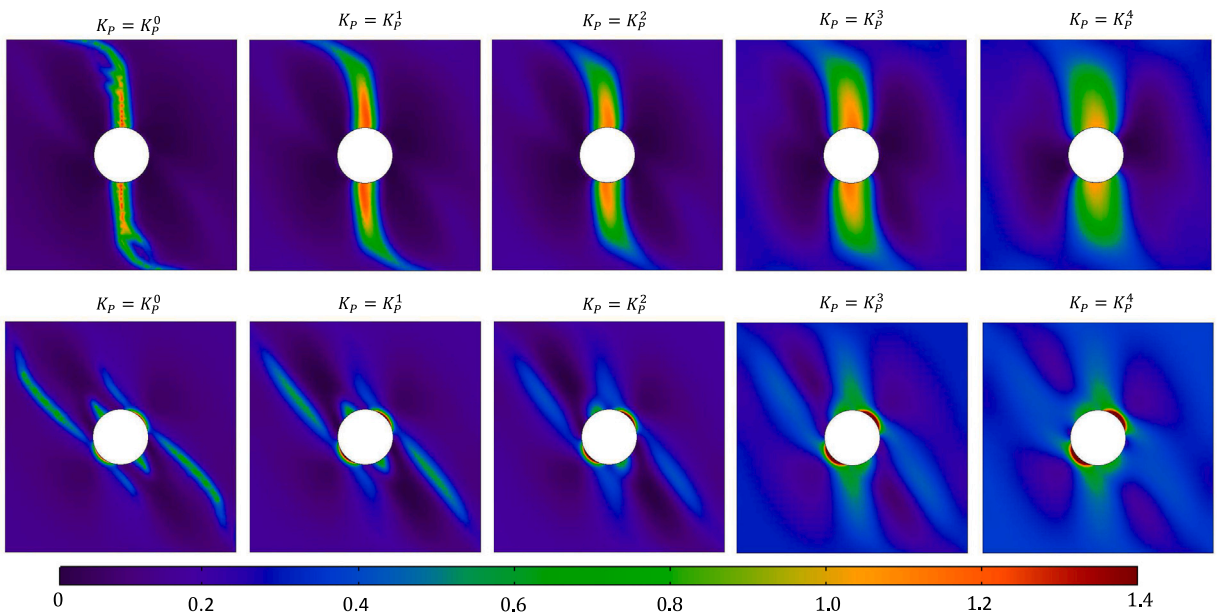

Fig. 30. Contour plots of dissipation W_D energy densities tension–shear (1st row) and shear–tension (2nd row) for $K_P = K_p^2$ and for the $\mathcal{P}_1$ set of parameters defined in Tables 1–2 to compare the last time-steps of the simulations.

leads to completely different states at the end of the loading otherwise characterized by the same overall deformed shape of the specimen and similar reaction force as exemplified in Fig. 30.

6. Conclusion

The key findings of the work reported here is that long-range (beyond nearest neighbor) mechanism must be included in continuum models based upon micro-macro identification derived from discrete models. Here, we have shown that by including at micro-scale additional pantographic grain-pair interactions that store elastic energy in response to strain gradients, we can control at macro-scale the thickness of the localization zones that form as failure (fracture) nucleates from certain prescribed weakness. This outcome is demonstrated via numerical simulation of localization nucleation and propagation in a plate with prescribed hole. The influence of the pantographic term is observed both in the case of single loading and in more complex experiments. We find completely different localization characteristics even for the same final deformed shape of the specimen. This localization strongly depends upon the loading-path and reflects the consequences of different loading history for each grain-pair direction at the microscale. The results illustrate the capabilities of the micro-macro identification based upon the granular micromechanics paradigm, which we have demonstrated models load path dependency that gives rise to evolving anisotropy and material chirality as well as growth of localization zones from location other than the prescribed weakness. Future outlooks of the present work include the applications of the present framework to the study of more complex loading conditions and materials, as well as the development of actual granular metamaterials with pantographic connections. For those parameters

related to damage dissipation energy there is a work in progress to find a proper way for their experimental validation.

Declaration of competing interest

The authors declare that they have no known competing financial interests or personal relationships that could have appeared to influence the work reported in this paper.

Acknowledgments

AM is supported in part by the United States National Science Foundation grant CMMI -1727433. This project has received funding from the European Union's Horizon 2020 research and innovation program under the Marie Skłodowska-Curie grant agreement No 899546.

References

Askes, Harm, Aifantis, Elias C., 2011. Gradient elasticity in statics and dynamics: an overview of formulations, length scale identification procedures, finite element implementations and new results. Int. J. Solids Struct. 48 (13), 1962–1990.

Askes, Harm, Metrikine, Andrei V., 2005. Higher-order continua derived from discrete media: continualisation aspects and boundary conditions. Int. J. Solids Struct. 42 (1), 187–202.

Babuska, Ivo, Oden, J. Tinsley, 2004. Verification and validation in computational engineering and science: basic concepts. Comput. Methods Appl. Mech. Engrg. 193 (36), 4057–4066.

Barchiesi, Emilio, Eugster, Simon R., Placidi, Luca, dell'Isola, Francesco, 2019. Pantographic beam: a complete second gradient 1D-continuum in plane. Z. Angew. Math. Phys. 70 (5), 1–24.

Barchiesi, E., Laudato, M., Di Cosmo, F., 2018. Wave dispersion in non-linear pantographic beams. Mech. Res. Commun. 94, 128–132.

Boutin, C., Giorgio, I., Placidi, L., et al., 2017. Linear pantographic sheets: Asymptotic micro-macro models identification. Math. Mech. Complex Syst. 5 (2), 127–162.

Brach, Stella, Tanné, Erwan, Bourdin, Blaise, Bhattacharya, Kaushik, 2019. Phase-field study of crack nucleation and propagation in elastic–perfectly plastic bodies. Comput. Methods Appl. Mech. Engrg. 353, 44–65.

Carcaterra, A., dell'Isola, F., Esposito, R., Pulvirenti, M., 2015. Macroscopic description of microscopically strongly inhomogeneous systems: A mathematical basis for the synthesis of higher gradients metamaterials. Arch. Ration. Mech. Anal. 218 (3), 1239–1262.

Carrara, Pietro, Ambati, Marreddy, Alessi, Roberto, De Lorenzis, Laura, 2020. A framework to model the fatigue behavior of brittle materials based on a variational phase-field approach. Comput. Methods Appl. Mech. Engrg. 361, 112731.

Chang, Ching S., Gao, Jian, 1995. Second gradient constitutive theory for granular material with random packing structure. Int. J. Solids Struct. 32 (16), 2279–2293.

Coutris, Nicole, Thompson, Lonny L., Kosaraju, Sai, 2020. Asymptotic homogenization models for pantographic lattices with variable order rotational resistance at pivots. J. Mech. Phys. Solids 134, 103718.

De Angelo, Michele, Placidi, Luca, Nejadsadeghi, Nima, Misra, Anil, 2020. Non-standard timoshenko beam model for chiral metamaterial: Identification of stiffness parameters. Mech. Res. Commun. 103, 103462.

Del Vescovo, D., Giorgio, I., 2014. Dynamic problems for metamaterials: review of existing models and ideas for further research. Internat. J. Engrg. Sci. 80, 153–172.

dell'Isola, F., Bucci, S., Battista, A., 2016a. Against the fragmentation of knowledge: The power of multidisciplinary research for the design of metamaterials. Z. Angew. Math. Phys. 67 (4).

dell'Isola, F., Giorgio, I., Pawlikowski, M., Rizzi, N., 2016b. Large deformations of planar extensible beams and pantographic lattices: heuristic homogenization, experimental and numerical examples of equilibrium. Proc. R. Soc. Lond. Ser. A Math. Phys. Eng. Sci. 472 (2185), 20150790.

dell'Isola, Francesco, Turco, Emilio, Misra, Anil, Vangelatos, Zacharias, Grigoropoulos, Costas, Melissinaki, Vasileia, Farsari, Maria, 2019. Force–displacement relationship in micro-metric pantographs: Experiments and numerical simulations. Comp. R. Méc. 347 (5), 397–405.

Fang, Jianguang, Wu, Chengqing, Rabczuk, Timon, Wu, Chi, Sun, Guangyong, Li, Qing, 2020. Phase field fracture in elasto-plastic solids: a length-scale insensitive model for quasi-brittle materials. Comput. Mech. 66 (4), 931–961.

Giorgio, Ivan, Ciallella, Alessandro, Scerrato, Daria, 2020a. A study about the impact of the topological arrangement of fibers on fiber-reinforced composites: some guidelines aiming at the development of new ultra-stiff and ultra-soft metamaterials. Int. J. Solids Struct. 203, 73–83.

Giorgio, Ivan, dell'Isola, Francesco, Misra, Anil, 2020b. Chirality in 2D cosserat media related to stretch-micro-rotation coupling with links to granular micromechanics. Int. J. Solids Struct. 202, 28–38.

Golaszewski, Maciej, Grygoruk, Roman, Giorgio, Ivan, Laudato, Marco, Di Cosmo, Fabio, 2019. Metamaterials with relative displacements in their microstructure: technological challenges in 3D printing, experiments and numerical predictions. Contin. Mech. Thermodyn. 31 (4), 1015–1034.

Jia, D., Ramesh, K.T., Ma, E., 2003. Effects of nanocrystalline and ultrafine grain sizes on constitutive behavior and shear bands in iron. Acta Mater. 51 (12), 3495–3509.

Joshi, Shailendra P., Ramesh, K.T., 2008. Rotational diffusion and grain size dependent shear instability in nanostructured materials. Acta Mater. 56 (2), 282–291.

Kumar, Aditya, Bourdin, Blaise, Francfort, Gilles A., Lopez-Pamies, Oscar, 2020. Revisiting nucleation in the phase-field approach to brittle fracture. J. Mech. Phys. Solids 142, 104027.

Maranganti, R., Sharma, P., 2007. A novel atomistic approach to determine strain-gradient elasticity constants: Tabulation and comparison for various metals, semiconductors, silica, polymers and the (ir) relevance for nanotechnologies. J. Mech. Phys. Solids 55 (9), 1823–1852.

Miehe, C., Teichtmeister, S., Aldakheel, F., 2016. Phase-field modelling of ductile fracture: a variational gradient-extended plasticity-damage theory and its micromorphic regularization. Phil. Trans. R. Soc. A 374 (2066), 20150170.

Misra, Anil, Nejadsadeghi, Nima, De Angelo, Michele, Placidi, Luca, 2020. Chiral metamaterial predicted by granular micromechanics: verified with 1D example synthesized using additive manufacturing. Contin. Mech. Thermodyn. 32 (5), 1497–1513.

Misra, Anil, Placidi, Luca, dell'Isola, Francesco, Barchiesi, Emilio, 2021. Identification of a geometrically nonlinear micromorphic continuum via granular micromechanics. Z. Angew. Math. Phys. 72 (4), 1–21.

Misra, A., Poorsolhjouy, P., 2015. Granular micromechanics model for damage and plasticity of cementitious materials based upon thermomechanics. Math. Mech. Solids 1081286515576821.

Misra, A., Singh, V., 2015. Thermomechanics-based nonlinear rate-dependent coupled damage-plasticity granular micromechanics model. Contin. Mech. Thermodyn. 27 (4–5), 787.

Mohsenizadeh, Mehrdad, Gasbarri, Federico, Munther, Michael, Beheshti, Ali, Davami, Keivan, 2018. Additively-manufactured lightweight metamaterials for energy absorption. Mater. Des. 139, 521–530.

Molnár, Gergely, Doitrand, Aurélien, Estevez, Rafaël, Gravouil, Anthony, 2020. Toughness or strength? Regularization in phase-field fracture explained by the coupled criterion. Theor. Appl. Fract. Mech. 109, 102736.

Nejadsadeghi, Nima, Placidi, Luca, Romeo, Maurizio, Misra, Anil, 2019. Frequency band gaps in dielectric granular metamaterials modulated by electric field. Mech. Res. Commun. 95, 96–103.

Nguyen, Hoang Thai, Pathirage, Madura, Cusatis, Gianluca, Bažant, Zdeněk P, 2020. Gap test of crack-parallel stress effect on quasibrittle fracture and its consequences. J. Appl. Mech. 87 (7), 071012.

Oberkampf, William L., Trucano, Timothy G., Hirsch, Charles, 2004. Verification, validation, and predictive capability in computational engineering and physics. Appl. Mech. Rev. 57 (5), 345–384.

Ouali, M. Ould, Poorsolhjouy, P., Placidi, L., Misra, A., 2021. Evaluation of the effects of stress concentrations on plates using granular micromechanics. Constr. Build. Mater. 290, 123227.

Placidi, Luca, Barchiesi, Emilio, Misra, Anil, 2018a. A strain gradient variational approach to damage: a comparison with damage gradient models and numerical results. Math. Mech. Complex Syst. 6 (2), 77–100.

Placidi, Luca, Barchiesi, Emilio, Misra, Anil, Timofeev, Dmitry, 2021. Micromechanics-based elasto-plastic-damage energy formulation for strain gradient solids with granular microstructure. Contin. Mech. Thermodyn. 1–29.

Placidi, Luca, Misra, Anil, Barchiesi, Emilio, 2018b. Two-dimensional strain gradient damage modeling: a variational approach. Z. Angew. Math. Phys. 69 (3), 56.

Placidi, Luca, Misra, Anil, Barchiesi, Emilio, 2019. Simulation results for damage with evolving microstructure and growing strain gradient moduli. Contin. Mech. Thermodyn. 31 (4), 1143–1163.

Polyzos, D., Fotiadis, D.I., 2012. Derivation of Mindlin's first and second strain gradient elastic theory via simple lattice and continuum models. Int. J. Solids Struct. 49 (3–4), 470–480.

Pook, Leslie Philip, 2000. Linear Elastic Fracture Mechanics for Engineers: Theory and Applications. WIT Press.

Rahali, Y., Giorgio, I., Ganghoffer, J.F., Dell'Isola, F., 2015. Homogenization à la Piola produces second gradient continuum models for linear pantographic lattices. Internat. J. Engrg. Sci. 97, 148–172.

Schwer, L.E., 2007. An overview of the PTC 60/V& V 10: Guide for verification and validation in computational solid mechanics. Eng. Comput. 23 (4), 245–252.

Seppecher, Pierre, Spagnuolo, Mario, Barchiesi, Emilio, Hild, François, Lekszycki, Tomasz, Giorgio, Ivan, Placidi, Luca, Andreaus, Ugo, Cuomo, Massimo, Eugster, Simon R., et al., 2019. Advances in pantographic structures: design, manufacturing, models, experiments and image analyses. Contin. Mech. Thermodyn. 31 (4).

Spagnuolo, Mario, Peyre, Patrice, Dupuy, Corinne, 2019. Phenomenological aspects of quasi-perfect pivots in metallic pantographic structures. Mech. Res. Commun. 101, 103415.

Tanné, Erwan, Li, Tianyi, Bourdin, Blaise, Marigo, J-J, Maurini, Corrado, 2018. Crack nucleation in variational phase-field models of brittle fracture. J. Mech. Phys. Solids 110, 80–99.

Timofeev, Dmitry, Barchiesi, Emilio, Placidi, Luca, Misra, Anil, 2020. Hemivariational continuum approach for granular solids with damage-induced anisotropy evolution. Math. Mech. Solids 26, 1–33.

TMS, The Minerals Metals & Materials Society (TMS), 2019. Verification & Validation of Computational Models Associated with the Mechanics of Materials. TMS, Pittsburgh, PA.

Tokaji, Keiro, Ogawa, Takeshi, Harada, Yukio, 1987. Evaluation on limitation of linear elastic fracture mechanics for small fatigue crack growth. Fatigue Fract. Eng. Mater. Struct. 10 (4), 281–289.

Triantafyllidis, Nicolas, Bardenhagen, S., 1993. On higher order gradient continuum theories in 1-D nonlinear elasticity. Derivation from and comparison to the corresponding discrete models. J. Elasticity 33 (3), 259–293.

Trippel, Antonina, Stilz, Maximilian, Gutmann, Florian, Ganzenmueller, Georg C, Hiermaier, Stefan, 2020. A device for characterizing rotational joints in metamaterials. Mech. Res. Commun. 104, 103501.

Turco, Emilio, 2019. Numerically driven tuning of equilibrium paths for pantographic beams. Contin. Mech. Thermodyn. 31 (6), 1941–1960.

Turco, Emilio, 2021. A numerical survey of nonlinear dynamical responses of discrete pantographic beams. Contin. Mech. Thermodyn. 1–21.

Turco, Emilio, Barchiesi, Emilio, dell'Isola, Francesco, 2021. A numerical investigation on impulse-induced nonlinear longitudinal waves in pantographic beams. Math. Mech. Solids 10812865211010877.

Turco, E., dell'Isola, F., Rizzi, N.L., Grygoruk, R., Müller, W.H., Liebold, C., 2016. Fiber rupture in sheared planar pantographic sheets: Numerical and experimental evidence. Mech. Res. Commun. 76, 86–90.

Turco, Emilio, Rizzi, Nicola Luigi, 2016. Pantographic structures presenting statistically distributed defects: numerical investigations of the effects on deformation fields. Mech. Res. Commun. 77, 65–69.

Wang, C., Qian, X., 2018. Heaviside projection based aggregation in stress constrained topology optimization. Internat. J. Numer. Methods Engrg. 115 (7), 849–871.

Yildizdag, Mustafa Erden, Tran, Chuong Anthony, Barchiesi, Emilio, Spagnuolo, Mario, dell'Isola, Francesco, Hild, François, 2019. A multi-disciplinary approach for mechanical metamaterial synthesis: a hierarchical modular multiscale cellular structure paradigm. In: State of the Art and Future Trends in Material Modeling. Springer, pp. 485–505.

Zheng, Xiaoyu, Lee, Howon, Weisgraber, Todd H, Shusteff, Maxim, DeOtte, Joshua, Duoss, Eric B, Kuntz, Joshua D, Biener, Monika M, Ge, Qi, Jackson, Julie A, et al., 2014. Ultralight, ultrastiff mechanical metamaterials. Science 344 (6190), 1373–1377.